Master's Thesis

Cosmic Muon Tracking with Micromegas Detectors and Neutron Source Characterisation

Faculty of Physics
Ludwig-Maximilians-Universität München

Eshita Kumar

Submitted in partial fulfilment of the requirements for the degree of M. Sc.
Supervised by Prof. Dr. Otmar Biebel

Master's Thesis

Spurrekonstruktion kosmischer Myonen mit Micromegas Detektoren und Charakterisierung einer Neutronenquelle

Fakultät der Physik
Ludwig-Maximilians-Universität München

Eshita Kumar

Submitted in partial fulfilment of the requirements for the degree of M. Sc.
Supervised by Prof. Dr. Otmar Biebel

Abstract

MICRO MEsh GAseous Structure (Micromegas) detectors are Micro-Pattern Gaseous Detectors (MPGDs) that have high rate capability due to the fast evacuation of positive ions and excellent spatial resolution due to a small-scale readout strip pitch. These detectors were chosen to be installed in the New Small Wheels of the ATLAS Experiment at CERN due to their capability of coping with the increased rates for the upcoming luminosity upgrade of the Large Hadron Collider (LHC), achieving high muon detection efficiency and high precision tracking.

These Micromegas detectors are part of the inner forward muon spectrometer, as a result of which they suffer from harsh background radiation of neutrons, photons and strongly ionising particles. To test the performance and resilience of such detectors in detecting cosmic muons under high background, a 2 m^2 Micromegas detector with four layers was irradiated by a 10 GBq Americium-Beryllium neutron source for a period of three years. In this thesis, the analysis performed on these measurements without background radiation and the final results obtained on the efficiency of the detectors in tracking cosmic muons will be discussed.

Furthermore, an intensive study on the characteristics of the neutron source used was carried out: measurements with shielding materials of varying thicknesses placed in front of the source were used to disentangle the detector response for gamma and neutron radiation. A Germanium detector was used in order to determine the intensity of gammas produced by the source. Following this, a Geant4 simulation to determine the interaction probability from the background radiation was performed. A comparison of the analysis of the detector output to the simulation results for the final charge obtained from the gammas and the neutrons is discussed.

Contents

Chapter 1

Introduction

Gaseous detectors are being planned and constructed in several accelerator facilities due to their robustness, good stability and energy resolution. They are also the best options for economically covering large detection area with low budget material. One of these gaseous detectors is the Micromegas (MICRO-MEsh GAseous Structure) detector developed by Y. Giomataris, (Giomataris et al. 1996) which are micro-patterned detectors that have high rate capability due to the fast evacuation of positive ions and excellent spatial resolution in the order of 100 μm, due to a small scale readout strip pitch. This is one of the key contributing factors due to which the Micromegas was selected to be installed in the New Small Wheel (NSW) Project of the ATLAS Experiment at CERN ("European Organization for Nuclear Research") (Stelzer 2016) for the high luminosity upgrade of the Large Hadron Collider (LHC).

The ATLAS experiment at LHC is a large, cylindrical, multi-purpose particle detector built symmetrically around the interaction point, which is the point where the two beams collide. Fig. 1.1 shows you the schematic image of the ATLAS detector. The muon system consists of three layers and the part of the muon system closest to the interaction point in the direction of the beam are the two so called Small-Wheels, which have a distance to the interaction point of 7 m and hence face the harshest background flux in the entire system.

With the upcoming high luminosity upgrade of the LHC, the Micromegas detectors have replaced the previously used Monitored Drift Tubes (MDTs) in the Small-Wheels, which are incapable of handling the increased high radiation background (Kawamoto et al. 2013). These Micromegas thus face a high rate of gamma and neutron flux in addition to the muon particles from the beam. Detector modules of four different types (manufactured by Germany (SM2), Italy (SM1), France (LM1), Russia and Greece (LM2)) were produced separately to fit the wheel structure. A part of the Micromegas detectors for this update (called "SM2 modules"), were designed and built by the German collaboration which LMU Munich is a

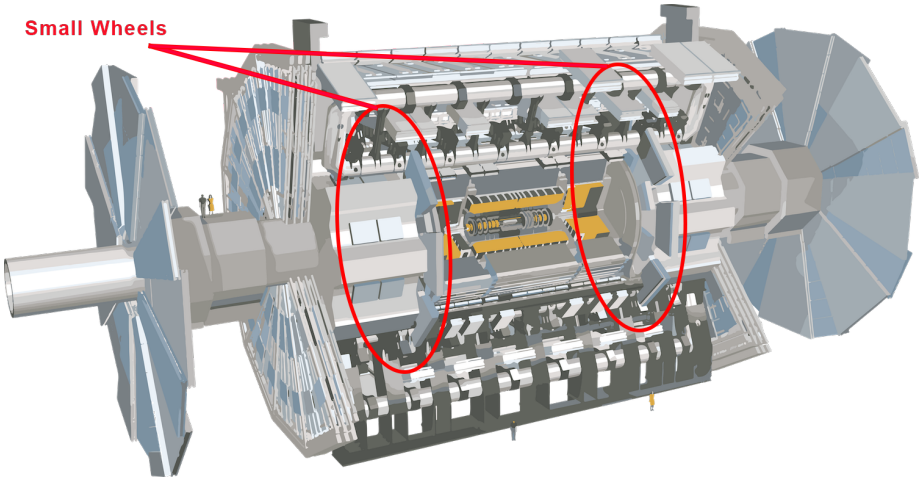

FIGURE 1.1: Schematic image of the ATLAS experiment with the Small Wheels circled in red. Image adapted from CERN[1].

member of. One of the spare modules from this production was used to study the performance of these detectors in order to better understand the detector efficiency and resilience.

A neutron source was placed in front of the detector for a period of three years to test the performance of the detector works under high background flux. The source was used as reference for the background irradiation is a high activity 10 GBq Americium-Beryllium neutron source, which emits MeV range gammas and neutrons. However, apart from the source's activity and neutron intensity, its specifications are unknown because it is an old source (>50 years of activity) and was obtained from another facility. Therefore, a characterisation study is necessary to fully understand its gamma intensity distribution.

For this thesis, a Germanium detector was used in order to obtain the intensity distribution of the neutron source. We use Geant4 (GEometry ANd Tracking) simulations to simulate the behaviour of the background radiation in the Micromegas detector and use the intensity distribution of the photons and neutrons to obtain the total number of electrons the detector would expect to reach the amplification region. This number must be proportional to the current drawn from the detector. The results of the characterisation and the simulation are discussed and finally compared to the measurements taken with the Micromegas detector.

[1] https://atlas.cern/Discover/Detector

Chapter 2

Interaction of Particles with Matter

In gaseous detectors, all particles are detected through their interaction with matter. Their interaction with matter differs based on the type and charge of the particle, which is explained more in the next few sections.

2.1 Bethe Bloch Equation for Charged Particles

For charged particles like muons, the dominating interaction process is ionisation where an electron may get kicked out, creating an electron-ion pair. Occasionally when a high energy transfer takes place, the ejected electron can further cause several ionisations, leaving an ionisation "trail". In some cases, wherein depending on the type of collision the particle undergoes, an electron may also get excited to a higher atomic bound state.

These interactions via excitation or ionisation of the atom leads to an energy loss of the traversing particle. The mean energy loss per distance travelled by the charged particle is described by the Bethe-Bloch equation (Cockcroft 1955)

$$-\left\langle \frac{dE}{dx} \right\rangle = 4\pi N_A r_e^2 m_e c^2 \rho \frac{Z z^2}{A\beta^2} \left(\frac{1}{2} \ln \left[\frac{2 m_e c^2 \beta^2 \gamma^2 T_m a x}{I^2} \right] - \beta^2 - \frac{\delta}{2} \right) \tag{2.1}$$

with N_A: Avogadro's constant, r_e: classical electron radius, m_e: mass of the electron, c: speed of light and the Lorentz factor $\gamma = 1/\sqrt{1-\beta^2}$, where the incoming particle has a velocity v, with $\beta = v/c$. The properties of the absorbing material include its density ρ, atomic number Z and atomic weight A with charge z in units of e. $T_{max} \approx 2 m_e c^2 \beta^2 \gamma^2$ is the maximum energy transfer to an electron, I is the mean ionisation potential of the material and δ is the Fermi density correction.

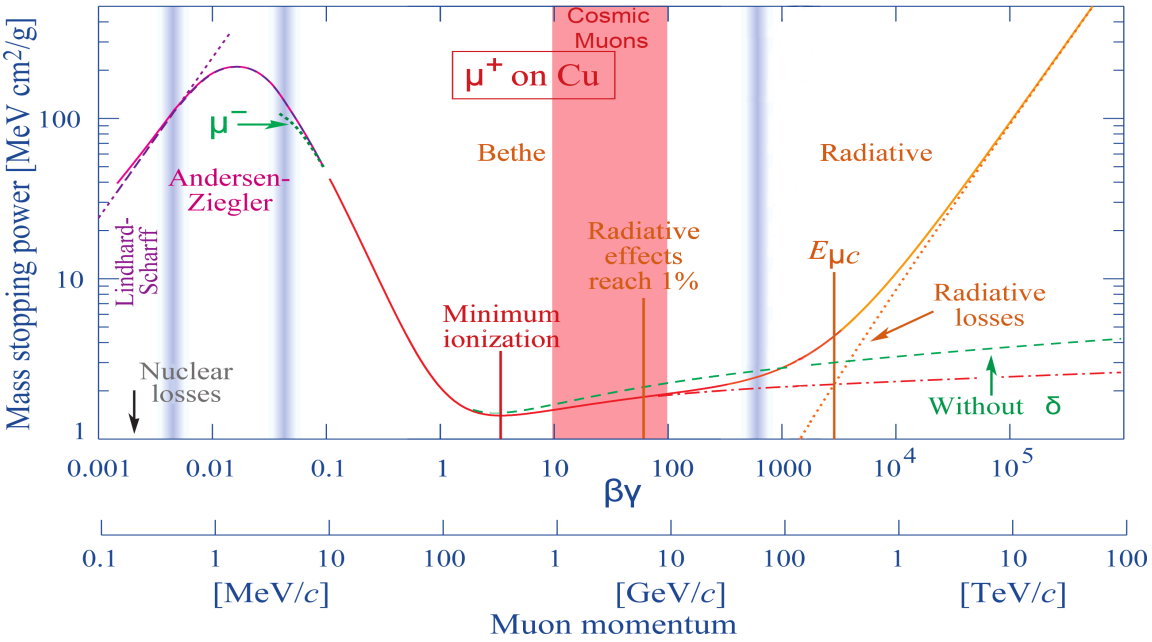

FIGURE 2.1: The stopping power of a positively charged muon as a function of its momentum and the $\beta\gamma$ values in copper. Figure adapted from (Tanabashi et al. 2018), with the particles of interest in this thesis: cosmic muons, indicated in red.

The formula shows that the ionisation loss is mainly depends on the velocity of the incoming particle and its charge. As seen in Fig.2.1, at low momenta ($\beta\gamma < 0.1$) the rate of the stopping power decreases proportionally to $1/\beta^2$. This explains why slower particles that stay in the proximity of atomic electrons for a longer time have a higher interaction probability. As the particles momentum increases ($\beta\gamma > 100$), the electric field around the particle flatten and increases its range of influence, resulting in a logarithmic rise that reaches a saturation value. These two conflicting effects create a minimum ionisation region ($\beta\gamma = 3$-4). Particles that have a mean ionisation energy loss in the range of the minimum are known as minimum ionising particles (MIPs). Cosmic muons having momenta in the 0.4-10 GeV/c range are MIPs with a small mean energy loss that is close to the minimum.

When a high energy loss takes place in a single interaction for incident particles that ionise the atoms of the material, electrons are ejected out of the atom with energies high enough to form their own ionisation trail. These electrons, known as δ-electrons, cause an asymmetry in the probability distribution of ionisation energy loss, giving it a tail toward high energies, forming a Landau distribution (Landau 1944). As a result, when a large energy transfer occurs, the mean energy

loss is much higher than the most probable value in that medium. This is more apparent in thin media due to high variations in energy loss processes due to fewer collisions, whereas in thicker absorbers, the probability distribution approaches a Gaussian function and the mean energy loss approaches the most probable value.

2.2 Energy Loss Mechanisms for Photons

Photons are charge neutral particles that undergo three main interaction processes: photoelectric absorption, Compton scattering and pair production, which are explained further in detail below. The total cross section of a photon in a material is given by

$$\sigma_{tot} = \sigma_{ph} + \sigma_{comp} + \sigma_{pair} \tag{2.2}$$

These competing processes dominate based on the energies of the photon and the atomic number Z of the absorber material as given in Fig. 2.2.

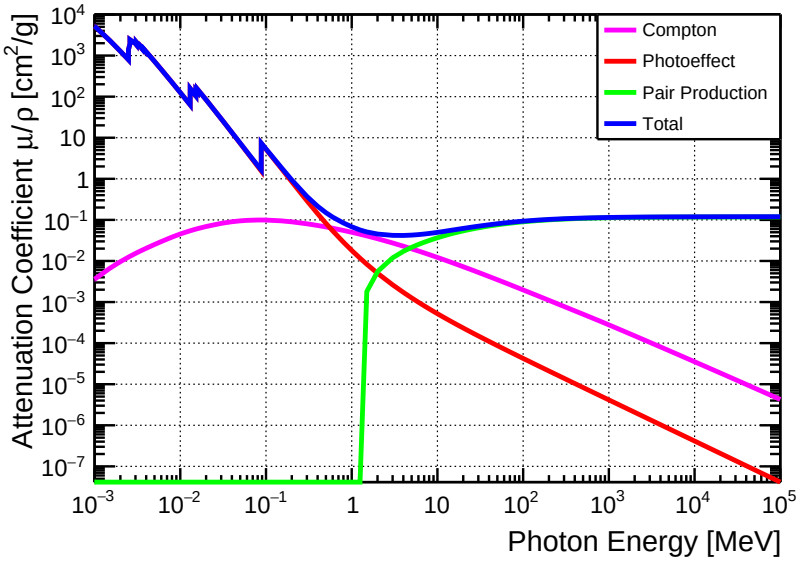

FIGURE 2.2: Mass attenuation coefficients μ/ρ plotted for different photon energies in the material Lead. The dominating interactions for photon energy in the range 10^{-3} to 10^5 MeV are given with the blue line indicating the total contribution from all interaction processes. Data taken from XCOM database (Berger M.J. 2010).

2.2.1 Photoelectric Effect

When an incident photon interacts with the entire atom, it transfers its entire energy to the bound electron of the atom and gets completely absorbed. Some of this energy is used to overcome the binding energy of the electron and the rest is converted into kinetic energy. This electron, often referred to as a photoelectron, is ejected from the atom and depending on its energy, further ionises or excites other atoms along its way. This interaction process dominates for the low energy gamma rays and the cross section can be approximately determined using (Davisson 1965)

$$\sigma_{ph} = \frac{16}{2}\sqrt{2}\pi r_e^2 \alpha^4 \frac{Z^5}{\gamma^{3.5}} \approx 3 \cdot 10^{12} \frac{Z^4}{E_\gamma^{3.5}}, \tag{2.3}$$

with $\gamma = E_\gamma / E_e$, where E_γ is the photon energy and E_e is the rest mass of an electron, r_e is the classical electron radius and α is the fine structure constant.

2.2.2 Compton Scattering

Compton effect is the incoherant scattering of the incident photon on interaction with a loosely bound electron of the atom. Unlike photoeffect, the incident photon only loses a fraction of its energy to the electron and gets scattered with the remaining energy. The electron is then kicked out of the atom with this fraction of energy after overcoming the binding energy. The cross section of Compton scattering can be determined using the differential Klein-Nishina formula given by (Klein and Nishina 1929)

$$\frac{d\sigma_{comp}}{d\Omega} = \frac{r_e^2}{2} \frac{1}{[1+\gamma(1-\cos\theta)]^2} \left(1 + \cos^2\theta + \frac{\gamma^2(1-\cos\theta)^2)}{1+\gamma(1-\cos\theta)} \right) \tag{2.4}$$

where Ω is the solid angle and θ is the angle of deflection. On integrating over $d\Omega$, we get the total probability of Compton scattering.

$$\sigma_{comp} = 2\pi r_e^2 \left[\frac{1+\gamma}{\gamma^2} \left(\frac{2(1+\gamma)}{1+2\gamma} - \frac{1}{\gamma} \ln(1+2\gamma) - \frac{1+3\gamma}{(1+2\gamma)^2} \right) \right] \tag{2.5}$$

Compton scattering is the dominant absorption mechanism for gamma rays in the intermediate energy range 100 keV to 10 MeV and thereafter decreases as the photon energy increases. The intensity distribution of the energy transferred to the recoil electrons can be determined using the Klein Nishina formula such that

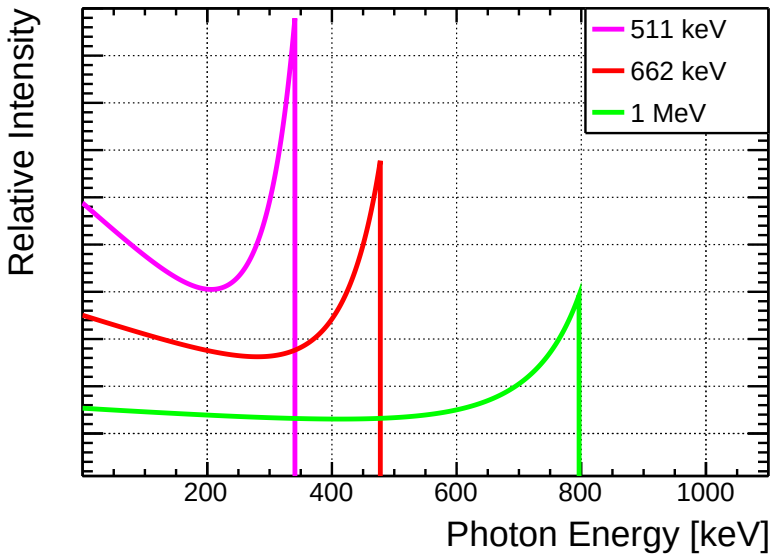

FIGURE 2.3: Compton intensity distribution of photon energies 511 keV, 662 keV and 1 MeV. The largest pulses from the Compton continuum form the Compton edge.

(Leo 1994)

$$\frac{d\sigma_{comp}}{dT} = \frac{\pi r_e^2}{m_e c^2 \gamma^2} \cdot \left[2 + \frac{s^2}{\gamma^2 (s-1)^2} + \frac{s}{1-s}\left(s - \frac{2}{\gamma} \right) \right], \tag{2.6}$$

where $T = E_\gamma - E_\gamma^{'}$, with $E_\gamma^{'}$ being the energy of the outgoing photon and $s = T/E_\gamma$. The relative intensity distribution for photons with different energies is shown in Fig. 2.3. The amount of energy lost by the photon is determined by the angle of deflection such that

$$E_\gamma^{'} = \frac{E_e}{1 + \gamma(1 - \cos\theta)} \tag{2.7}$$

where no energy is transferred as θ approaches zero and the maximum amount of energy is lost when $\theta = 180^\circ$ such that

$$E_{edge} = E_\gamma \left(1 - \frac{1}{1 + \frac{2E_\gamma}{E_e}} \right) \tag{2.8}$$

and the photon cannot transfer any more energy through Compton scattering, resulting in a sharp cut off at this energy, giving rise to the name Compton edge.

2.2.3 Pair Production

Pair production occurs for higher photon energies (E_γ> 1.022 MeV) under the influence of strong electromagnetic field near the nucleus. This interaction results in the creation of an electron-positron pair, with the nucleus receiving a small amount of recoil energy to conserve momentum. The minimum energy required to create an electron-positron pair is 1.022 MeV, and any excess energy is converted into kinetic energy and shared between the pair.

This kinetic energy is quickly absorbed, and the positron annihilates the electron, resulting in two 511 keV gammas. If only one of the gammas interacts with the detector, a single escape peak is formed in the spectrum, with the energy deposited in the detector being the photopeak of the original photon minus 511 keV. Similarly, if both the gammas escape, a double escape peak can be observed with the energy at original photon energy minus 1.022 MeV.

As can be seen from Fig. 2.2, the cross section for pair production is zero until the energy threshold at 1.022 MeV which rises till it reaches energies above 100 MeV, where it remains constant. This is given by (Rossi and Greisen 1941)

$$\sigma = \frac{7A}{9X_o N_A} \tag{2.9}$$

where A is the atomic mass of the target, N_A is Avogadro's number and X_o is the radiation length.

2.3 Neutron-Matter Interaction

Neutrons are neutral particles that interact with the nucleus of the atom via strong force, unlike the photons which interact via Coulomb interactions with the electrons of the atom. Neutron interactions are scarce due to the short range of this force and hence are very penetrating particles. Fast neutrons lose their kinetic energy with each collision, both elastic and inelastic until it reaches thermal equilibrium with the material atoms. The total cross section of neutrons in a material is given by (Leo 1994)

$$\sigma_{tot} = \sigma_{elastic} + \sigma_{inelastic} + \sigma_{neutron\ capture} + ... \tag{2.10}$$

with elastic and inelastic scattering being the dominant interactions in the 1-10 MeV energy range. This section will explore more on how these interactions take place.

2.3.1 Elastic Scattering

On collision with a nucleus at rest, the velocity of fast neutrons (>100 keV) in the center of mass system is (Leo 1994)

$$\nu_{com} = \frac{A}{A+1}\nu_o \tag{2.11}$$

where the mass is written in terms of neutron mass, i.e. $m_{neutron}$=1 and $m_{nucleus}$=A, A being the atomic mass number. On the other hand, the nucleus acquires a velocity

$$V = \frac{1}{A+1}\nu_o \tag{2.12}$$

The corresponding velocity of the neutron in the laboratory frame is given by

$$\nu_{lab}^2 = (\nu_{com})^2 + V^2 - 2\nu_{com} \cdot V \cos(\pi - \theta_{com}) \tag{2.13}$$

where the center of mass scattering angle is denoted by θ_{com}. On plugging in the values of eq. 2.11 and eq. 2.12 into eq. 2.13, we get

$$\nu_{lab}^2 = \left(\frac{A}{A+1}\right)^2 \nu_o^2 + \left(\frac{1}{A+1}\right)^2 \nu_o^2 - 2\frac{A}{(A+1)^2}\nu_o^2 \cos(\pi - \theta_{com}) \tag{2.14}$$

To estimate the limits on the energy range of the scattered neutron using kinetic energy E=$\frac{1}{2}$mv^2, we get

$$\frac{E}{E_o} = \left(\frac{v_{lab}}{v_o}\right)^2 \tag{2.15}$$

$$\frac{E}{E_o} = \frac{A^2 + 1 + 2A\cos\theta_{com}}{(A+1)^2} \tag{2.16}$$

On applying the limits cos θ_{com}=$\pm$1, the energy of the scattered neutron is limited to

$$\left(\frac{A-1}{A+1}\right)^2 < E < E_o \tag{2.17}$$

This is the dominant interaction for most nuclei and neutron energies and the energy transfer increases for masses closer to the neutron mass since the lighter the nucleus, the more recoil energy it absorbs from the neutron. As a result, lower atomic mass materials such as water and plastic are effective moderators used to slow down neutrons. The cross section for elastic scattering can be considered approximately constant for most materials, with an example material copper given in Fig. 2.4.

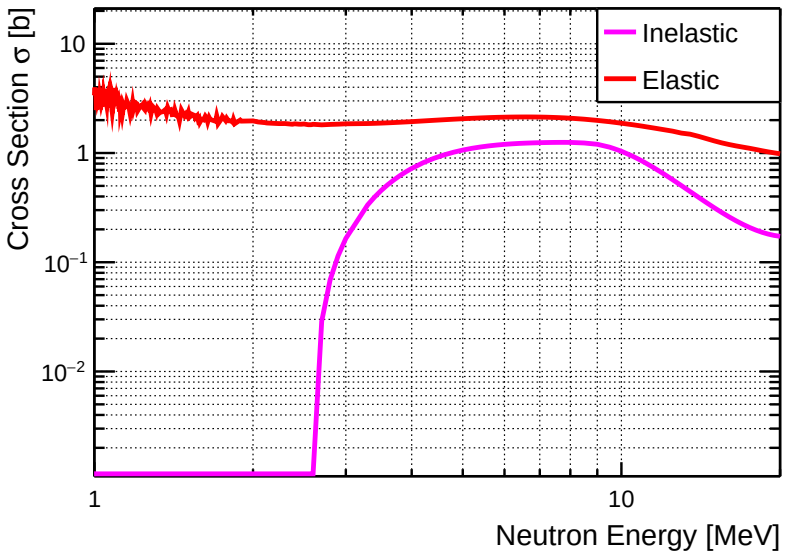

FIGURE 2.4: Cross sections of fast neutrons in the energy range 1-10 MeV in copper for the two dominating processes in this region: elastic and inelastic scattering.

2.3.2 Inelastic Scattering

In an inelastic scattering reaction between an incident neutron and a target nucleus, the original neutron is absorbed by the recoiling nucleus and a new neutron of a lower kinetic energy is re-emitted, while the nucleus remains in the excited state. Unlike elastic scattering, the total kinetic energy of the system is not conserved due to the excited nucleus. The nucleus is de-excited to the ground state via radiative transition, leading to the emission of one or more gammas.

Inelastic scattering is a threshold reaction where the threshold energy must be greater than the energy of the first excited state of the nucleus. This also means that hydrogen nuclei do not undergo any inelastic scattering since they do not have any excited states while the other lighter nuclei have a relatively small cross section. Inelastic collisions with heavy nuclei are useful in moderating neutrons at high energies.

Chapter 3

Theory and Working Principle of Micromegas Detectors

3.1 Theoretical Background

3.1.1 Drift and Mobility of Charge Carriers in Gas

Charged particles interact in gas via Coulomb scattering. High energetic particles mainly undergo ionisation (described in Section 2.1), creating electron-ion pairs in the gas. If no electric field is applied in this region, electron-ion pair recombination will dominate. On applying an electric field, the charge carriers are separated wherein the electron drifts towards the anode and the ion towards the cathode. The average velocity of the ion depends on its mobility μ^+, the strength of the electric field $\vec{E}$ and pressure p of the gas, given by (Townsend 1910)

$$v_d^+ = \mu^+ \cdot \vec{E} \cdot \frac{p_0}{p}, \tag{3.1}$$

where p_0/p is the pressure of the gas normalised to standard pressure. While the mobility of ions is mostly independent of field strength unless at high electric fields, the mobility of electrons is strongly dependent on the energy of electrons and by extension on the electric field. Because of their lighter mass, they have a larger mean free path, resulting in a mobility three orders of magnitude higher than ions. The electron drift velocity is then given by (Kleinknecht 1998)

$$v_d^- = \frac{e}{m_*}\vec{E}\tau(E,\epsilon), \tag{3.2}$$

with $\vec{E}$ being the field strength, τ being the time between two collisions and m_* being the effective mass of the electron. The interaction cross section is strongly

dependent on the energy of the electron and reaches a minimum for electrons whose wavelength $\lambda = \text{hp}$ approaches molecular dimensions. This effect, known as the Ramsauer effect (Ramsauer 2006), causes a large variation in the interaction cross sections of the electron with noble gases. The drift velocity is thus highly influenced by the exact composition of the gas, meaning that even small "impurities" to the noble gas will dramatically change the fractional energy loss, increasing the drift velocity by large factors since the number of electrons with energies close to this Ramsauer minimum increases and the average cross section decreases (Blum, Rolandi, and Riegler 2008). Gases like CO_2 or CH_2 can be added to the Argon gas in the detector to increase the effective drift velocity of electrons.

3.1.2 Townsend Avalanche in Gases

The charge $\sigma(10^{-18}\,\text{C})$ produced by the ionising particle is too small to be read out by the electronics of the detector. Hence, an amplification process is needed to amplify the signal from the particle and this is done using the Townsend avalanche.

On applying a strong electric field, these electrons gain kinetic energy above the ionisation energy of the molecules in the gas, resulting in further ionisation processes. Taking λ to be the mean free path of an electron in the gas with an applied electric field $\vec{E}$, if the kinetic energy gain is reached within the mean free path, the electron can ionise at every collision, thus creating an exponential amplification process called the Townsend amplification, described by (Kleinknecht 1998)

$$dN(x) = \alpha N_o dx \tag{3.3}$$

where N_o is the initial number of electrons and $\alpha = 1/\lambda(\vec{E})$ is the first Townsend coefficient. After a distance x traversed by the primary electron, we obtain a total number of electrons $N(x)$:

$$N(x) = N_o \cdot \exp(\alpha x) \tag{3.4}$$

Then the multiplication factor G i.e the gas gain is given by

$$\begin{aligned} G &= \frac{N(x)}{N_o} \\ G &= \exp(\alpha x) \end{aligned} \tag{3.5}$$

The coefficient α is determined by the excitation and ionisation cross sections of the gas atoms and is affected by the electric field $\vec{E}$ and gas density n. Hence,

no fundamental expression exists for α and it must be measured for every gas mixture. Nevertheless, an empirical relation for the first Townsend coefficient (Townsend 1910) can be determined based on field strength $\vec{E}$, temperature of the gas T and pressure of the gas P, such that

$$\alpha = A \cdot n \cdot \exp\left(- \frac{B \cdot n}{\mid \vec{E} \mid} \right) \tag{3.6}$$

where the parameters $A = A_o k_B$ and $B = B_o k_B$ are gas dependent constants and n is the gas density given by the ideal gas law

$$n = \frac{P}{k_B T} \tag{3.7}$$

Mean parameters of A = (111.2 $\pm$0.6) K/(bar μm) and B = (2196 $\pm$7) K V/(bar μm) have been estimated for an Ar:CO_2 93:7 vol.% gas mixture (Bortfeldt 2014). Then, using eq. 3.5 and eq. 3.6, we can estimate the gas gain G to be

$$G = \exp\left[A \cdot n \cdot \exp\left(- \frac{B \cdot n}{\mid \vec{E} \mid} \right) \cdot x \right] \tag{3.8}$$

Since the drift velocity of electrons is significantly higher than that of ions, the avalanche electrons are well separated from the positive ions in space. Thus, as these electrons begin to collect at the anode, the ions drift a short distance from their point of production, creating a space-charge effect. Despite the magnitude of the applied voltage, this space-charge effect lowers the actual electric field and slows the avalanche growth. This limits the gas gain from exponentially rising and is defined by the Raether limit of $\alpha x \approx 20$ (Raether 1964). On exceeding the Raether limit, a conducting plasma between the anode and cathode can equalise the voltage between the two electrodes. Quenching gases are used to suppress the additional charge-creation by capturing UV-photons created during these avalanches. In Micromegas detectors, a gas gain of $5 \cdot 10^3$ to 10^4 is expected (Iodice 2015).

3.2 Working Principle of Micromegas Detectors

The Micromegas detector is a gas-filled three-planar structure consisting of a cathode on the top and a segmented readout anode at the bottom, with a stainless steel micromesh in between dividing it into two distinct regions as can be seen in Fig.

3.1: the drift region, typically 5 mm between the cathode and the mesh with a potential difference between the two creating an electric field ranging from a couple hundred V/cm up to 1 kV/cm, and the amplification region, approximately 0.12 mm between the mesh and the resistive anode with an electric field in the order of 50 kV/cm. The gas mixture used for measurements in this thesis is Ar:CO_2 in a volume ratio 93:7%, where CO_2 is used as a quenching gas.

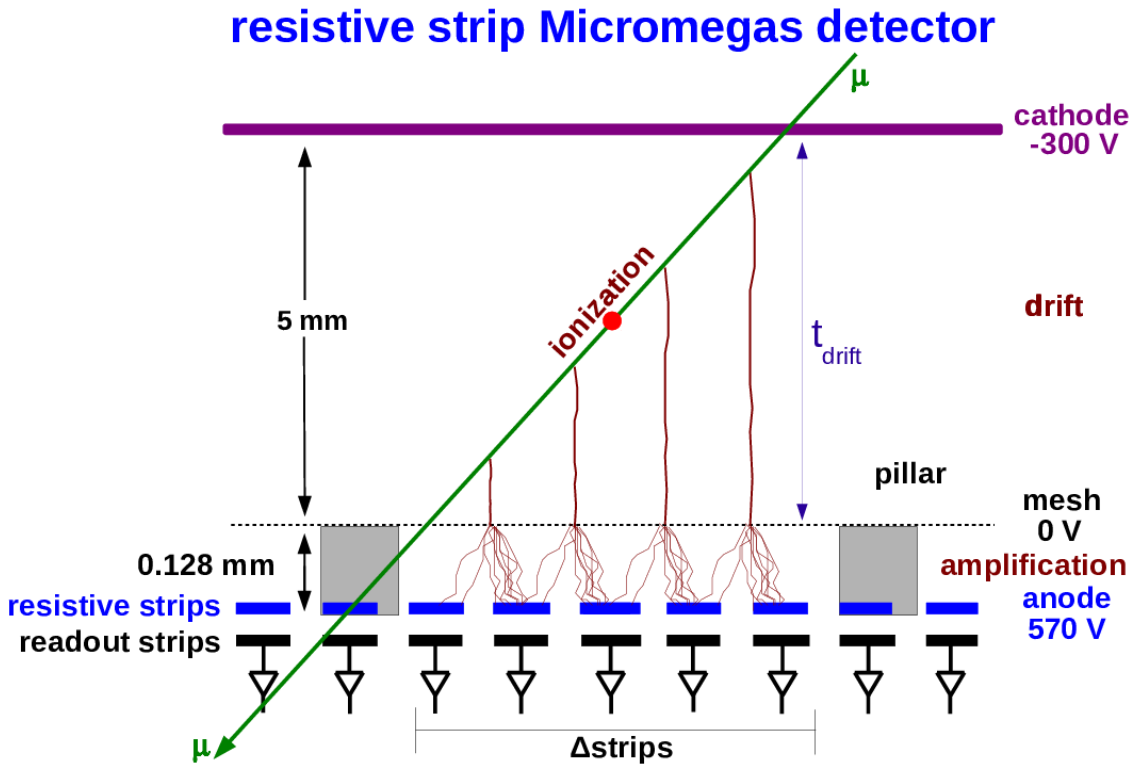

FIGURE 3.1: Typical design of a resistive strip Micromegas detector. A muon is traversing through the detector, ionising gas atoms in the drift region, where the electrons drift towards the amplification region due to a small electric field in the order of $\sim$ 1 kV/cm. A high electric field in the order of $\sim$ 50 kV/cm is applied between the mesh and the resistive anode, resulting in Townsend avalanches. These electrons are collected on the resistive strips and coupled capacitively to the readout strips. Image taken from (Lösel 2017).

According to the Bethe-Bloch equation (eq. 2.1), a charged muon loses energy as it traverses the detector, ionising the Argon atoms along its path. These electron-ion pairs are separated with the help of the electric field. The electron is funnelled through the mesh following the increasing electric field lines towards the amplification region, whilst the ion drifts to the cathode. Ideally, all electrons enter

the amplification area and are multiplied by an avalanche before being collected on the anode strips. The electron mesh transparency depends on the ratio of the amplification to the drift field and can reach up to more than 95% for an electric field in the amplification zone that is 50–100 times greater than in the drift region (Stelzer 2016).

Once in the amplification region, these electrons gain enough energy to undergo multiple secondary ionisations, leading to Townsend avalanches. This exponentially increases the number of electrons produced from the primary ionising particle. If the amplification voltage exceeds the Raether limit, a voltage breakdown can occur due to discharges, causing a dead time in the detector where it is unresponsive to incoming particles.

To overcome this occurrence, the detector is operated at voltages below the Raether limit. CO_2 is used as a quenching gas to minimise still occurring discharges to a small region, a layer of resistive strips is placed on top of the readout copper strips. The signal accumulated on the resistive strips is collected through capacitive coupling on the readout strips. The readout strips on the anode are printed parallel to each other with a strip pitch of 0.425 mm to detect the signal. These resistive Micromegas detectors as a result have excellent spatial resolution in the order of 100µm per detector layer (Flierl 2018). Due to the small amplification gap, these detectors have a dead-time of $\sim$100 ns, which is calculated using the drift time of the ions towards the mesh and the subsequent evacuation of positive ions (Kawamoto et al. 2013).

3.3 Signal Processing

3.3.1 Readout Electronics and Software

The electronics used to readout and digitise the charge collected at the readout strips is called the Scalable Readout System (SRS) (Martoiu et al. 2013), which has been developed by the RD51 collaboration[2]. A schematic view of the components in an SRS can be seen in Fig. 3.2. The SRS, as the name suggests, provides a standard back-end readout that can be utilised to scale to large systems while the front-end electronics is chosen by the suitability of the detector system used.

The first component of the SRS is the front-end chip whose purpose is to amplify and shape the signal received directly from the detector readout strips. The detector set-up for this thesis used the APV25 ASIC (Application Specific Integrated Circuit), which is a radiation-tolerant, low-noise analogue readout chip with 128

[2] www.cern.ch/rd51-public

electronic channels equipped with a pre-amplifier (Fig. 3.3). These chips were developed for the silicon strip detectors in the Compact Muon Solenoid (CMS) experiment at the LHC (Jones 2001). The charge collected from the readout strips is integrated into time intervals of 25 ns.

The ASIC chips are mounted on a hybrid board, which includes additional protection circuits against excessive input currents caused by discharges in the detector. These hybrid boards transmit the data via HDMI cables to an analogue to digital converter (ADC) card; this card digitises the analogue data. Two hybrid boards can be connected together, one acting as a master and the other as a slave,

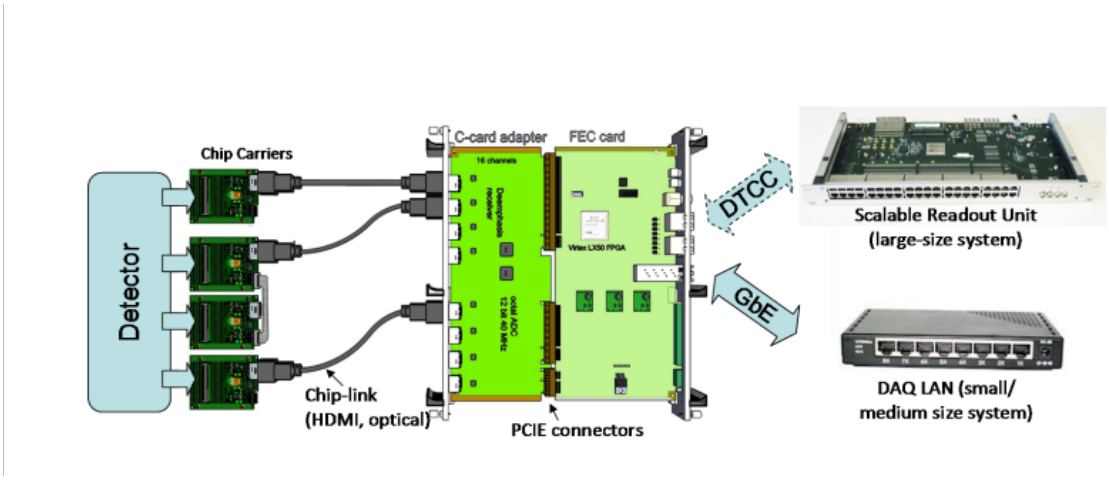

FIGURE 3.2: Schematic picture of the Scalable Readout System. The figure is taken from (Martoiu et al. 2013). Image taken from (Martoiu et al. 2013).

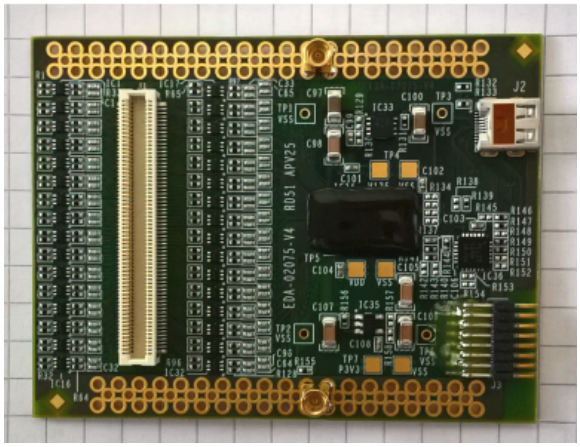

FIGURE 3.3: Image of a master APV25 hybrid board with safety circuits and a master-slave connector. Image taken from (Flierl 2018).

with the master board connected to the ADC card via a single HDMI cable. The ADC card is connected to a Front-End Concentrator (FEC) card which is used to communicate to the data acquisition computer via Gigabit Ethernet. A total of 8 HDMI cables can be connected to a single ADC card, which means a total of 16 hybrid boards are allowed in a stand-alone FEC system. If the system requires more channels, one or more Scalable Read-out Units (SRU) can be installed, which can be connected to up to 40 FEC cards (Jones 2001). In this thesis, 2 FEC cards with 16 APVs each are used, which are connected to the SRU that synchronises the two data streams to the data acquisition PC for all the measurements with the Micromegas detector.

3.3.2 Signal Reconstruction

This section focuses on the different methods of position and time reconstruction of the signals. The main C++ framework used for the fitting and analysis of signals received by the Micromegas readout electronics was developed by Vogel (Vogel 2024) and has been further adapted in this thesis.

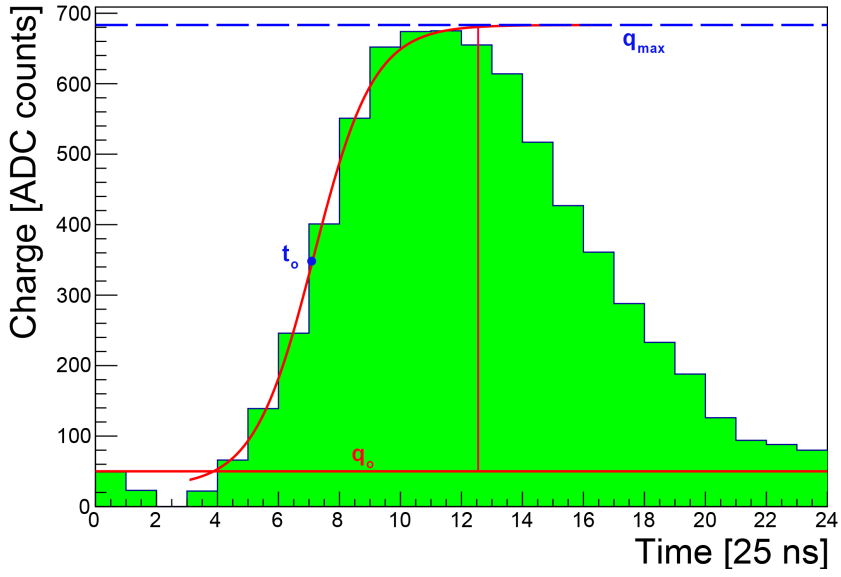

FIGURE 3.4: Typical signal from a cosmic muon traversing a Micromegas detector processed from an APV25 front end chip. The signal is fit to an inverse Fermi function which allows for an extraction of the charge q_{max} and timing t_o of the signal.

For a muon passing perpendicularly through the detector, the signal from the electron avalanches is usually collected over 2 to 4 strips, due to the diffusion of

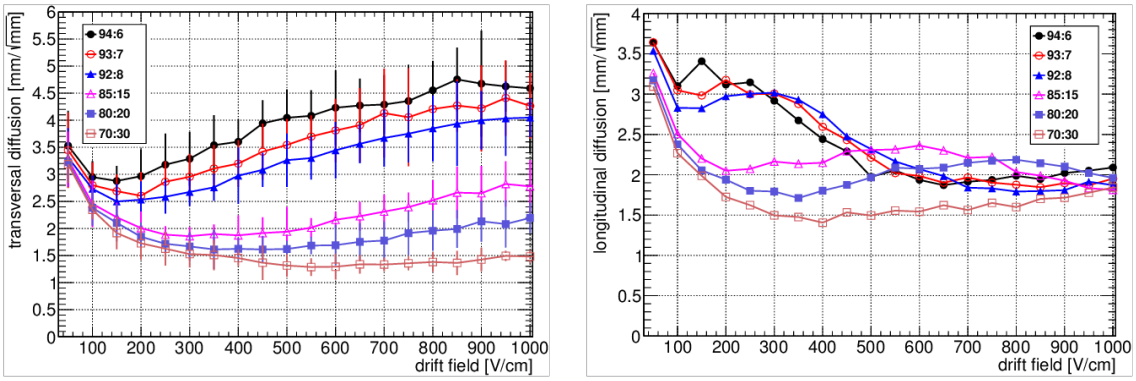

FIGURE 3.5: Simulated transverse and longitudinal diffusion respectively for different combinations of Ar:CO_2 at 20°C and 960 mbar as a function of the drift field. The electron distribution is diffused due to the statistical interaction with the gas atoms. Diffusion mainly depends on the drift field and the gas mixture used. Plots taken from (Herrmann 2019).

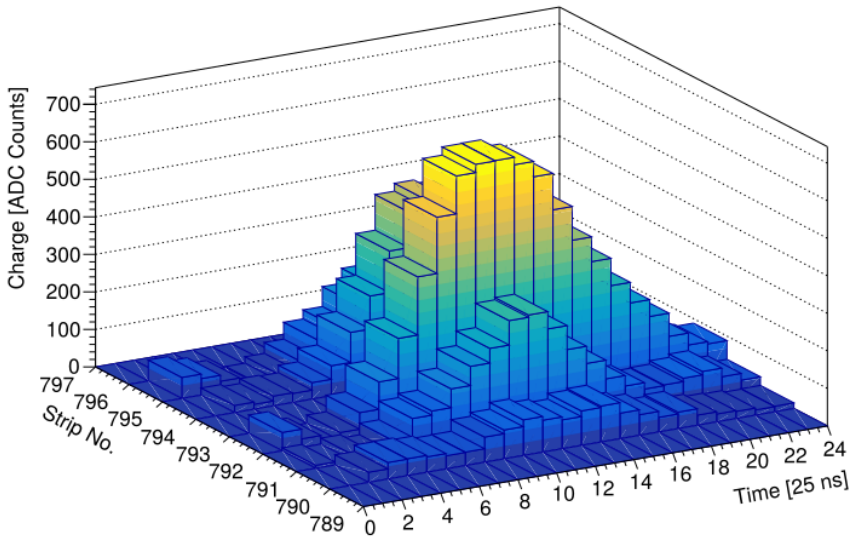

FIGURE 3.6: A group of good signals over multiple strips in a Micromegas detector, forming a "cluster". The analysis takes into consideration signals with dead strips and doesn't cut on these events.

the electrons which is dependent on the electric field, the gas mixture used (Fig. 3.5), the width of the amplification region as well as the strip pitch (Kleinknecht 1998). The strip signals are amplified and shaped by the APV25 front-end chip

which allows for the extraction of the charge and timing information of the signal from each strip (Fig. 3.4). A muon signal can be characterised by the fast rise of the electrons (due to their high mobility) followed by the ions as given in Fig. 3.4 The signal is fit with an inverse Fermi function given by

$$Q(t) = \frac{q_{max}}{1 + \exp\left(\frac{t_o - t}{\Delta t}\right)} + q_o \tag{3.9}$$

where q_{max} is the maximum of the signal height and q_o is the offset from the baseline to the zero value of the ADC. The rise time is given by Δt and the point of inflection by t_o. The timing information of the signal can be extracted from t_o due to the fast rise of the electrons. Since the detectors used here are proportional counters, the total charge q_{max} is proportional to the amount of energy deposited in the drift region. A collection of responding neighbouring strips receiving good signals forms a cluster, which is considered to contain all the information of a single particle as shown in Fig. 3.6.

3.3.3 Centroid Position Reconstruction

The signal from a single particle is collected across several readout strips, and the charge is typically Gaussian distributed for perpendicular tracks due to the transverse diffusion of the electrons in the gas (see Fig. 3.7). The particle position can be reconstructed by taking the weighted mean of the charge distribution corresponding to a cluster, given by

$$x_{centroid} = \frac{\sum\limits_{strips} x_{strip} \cdot q_{strip}}{\sum\limits_{strips} q_{strip}} \tag{3.10}$$

where x_{strip} is the position of the center of the strip and q_{strip} is the charge detected on that strip. This is known as the centroid or centre of gravity method, which reconstructs the position of the particle along the middle of the drift region. However, the particles of interest in this thesis are cosmic muons, such that the angular spectrum of cosmic muons results in a non-homogeneous ionisation along its track. This leads to a degradation in the accuracy of position reconstruction to the actual particle position. For inclined tracks, another method for position reconstruction is implemented, which is explained in the next sub-section.

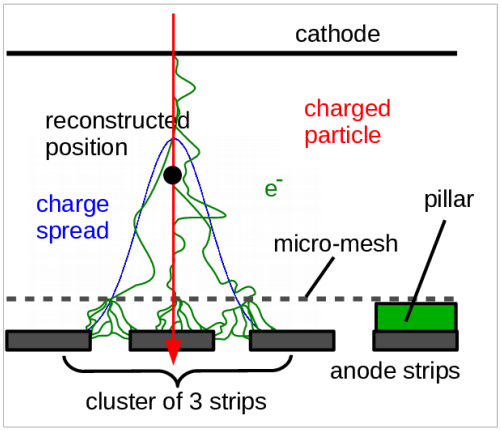

FIGURE 3.7: A charged particle (red) passing through the Micromegas detector creates electron-ion pairs along its path. These electrons (green) drift towards the amplification region where they are amplified in Townsend avalanches and get collected by the anode strips. For a perpendicularly incident particle the charge is typically Gaussian distributed (blue line) over a cluster of more than 2 strips, depending on the transverse diffusion of the electrons in the drift region. Figure taken from (Klitzner 2019).

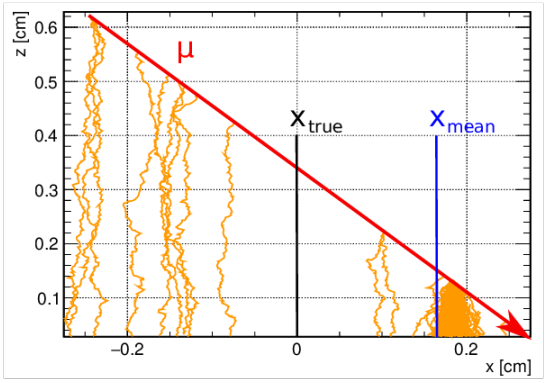

FIGURE 3.8: For an inclined track, more than two anode strips collect charge. The electrons created near the mesh reach the amplification region much faster than the ones created near the cathode. The inhomogeneous primary ionisation is given by the Landau shape of the energy loss. A Garfield++ simulation of a 2 GeV muon passing through the 6 mm drift region of the detector filled with Ar:CO_2 in 93:7 vol.% under an angle of $\theta = 40°$ and a drift field strength of 500 V/cm. Figure taken from (Klitzner 2019).

3.3.4 Time Corrected Charge Weighted Position Method

For tracks entering the detector at an inclination, more than two strips will collect the charge from a single particle and will lose their Gaussian shape. The signal from the electrons produced closer to the mesh will reach the amplification region almost instantaneously and much faster than the ones created at the beginning of the drift region near the cathode. An inhomogeneous ionisation along the muon path is defined by the Landau-like energy deposit of the minimum ionising particle in the thin detector medium. For inclined tracks, the position reconstruction of the cluster is at the centre of the drift gap as in Fig. 3.8.

For tracks with an inclination greater than 5°, a time corrected charge weighted position reconstruction method is used, developed by Flierl (Flierl 2018) which

utilises the homogeneous drift velocity of electrons in the drift region. The position in the z-plane can be determined using the timing of the charge weighted centroid position t_{cen} such that

$$t_{cen} = \frac{\sum_{i=0}^{n} q_i \cdot t_i}{\sum_{i=0}^{n} q_i} \tag{3.11}$$

where q_i and t_i are the charge and timing information of all the strips in a cluster. A timing offset can be determined from the mean signal timing $\Delta t = t_{mid} - t_{cen}$. The value of the parameter t_{mid} corresponds to the middle of the drift gap and is dependent on the drift velocity v_D, the drift gap width Δz given by

$$t_{mid} = \frac{\Delta z}{2 \cdot v_D} \tag{3.12}$$

Δt translates into a shift in the centroid position in z-direction and the corresponding shift in the read-out direction Δx can be then described by

$$\Delta x = \Delta t \cdot v_D \cdot \tan(\theta) \tag{3.13}$$

The track angle θ is given by either the reconstruction of the track shown in Fig. 3.8 using the timing information of the strips in a cluster or by the use of external reference detectors or is simply known, as in the case for ATLAS detectors where all the particles are created at the interaction point of the LHC bunches. In this thesis, the angle θ is determined using the reference detector layers and is explained more in detail in Section 4.3.

Chapter 4

Cosmic Muon Tracking using a Micromegas Detector

4.1 Motivation: Long Term Irradiation Studies

To test the stability of the Micromegas detectors under high background radiation, one of the spare chambers from the ATLAS NSW upgrade was used. This module set-up, given in Fig. 4.1, was consecutively irradiated with a high activity Americium-Beryllium source (see Section 5.1), placed immediately in front of the upstanding detector, for a total period of almost three years (Vogel et al. 2023).

The accumulated charge from the irradiation corresponds to multiple years in the working environment at ATLAS, depending on the distance from the centre of the source. The gas mixtures used during this period were Ar:CO_2 93:7 vol% for one year and the ternary mixture Ar:CO_2:iC_4H_{10} in 93:5:2 vol% for the remaining duration. The isobutane enriched gas mixture was used to mimic the ATLAS working conditions of the Micromegas detectors installed in the NSW of ATLAS since it showed better stability of the high amplification voltage, reducing the created discharges significantly (Vogel 2022).

In this thesis, measurements of the Micromegas detector were taken after the long-term irradiation studies to check the performance and efficiency of the detectors after having faced harsh background radiation. For the first round of measurements, the detector was flushed with Ar:CO_2, followed by the ternary mixture Ar:CO_2:iC_4H_{10} for the second set of measurements. The set-up, procedure of track reconstruction and performance results are discussed in the sections below.

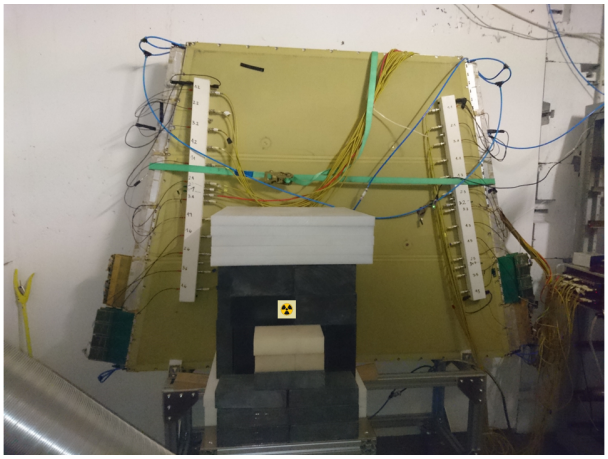

FIGURE 4.1: Long-Term Irradiation set-up for the Micromegas module with an Am-Be source placed in front with lead and plastic shielding.

4.2 Experimental Set-up

The measurements in this thesis are taken with the detector set-up as shown in Fig. 4.2. The set-up includes two 40 $\times$ 80 cm^2 scintillators used for triggering on cosmic muons, with the Micromegas SM2 module (see Chapter 1) placed between them. An event is considered when a cosmic muon triggers both the scintillators in coincidence. The angle of acceptance Φ for the cosmic muons hitting the scintillators can be determined using

$$\Phi = tan^{-1}\left(\frac{w_{sci}}{\Delta z}\right) \tag{4.1}$$

where w_{sci} is the width of the scintillator's sensitive region and Δz is the distance between the two scintillators. With Δz having an approximate distance of 80 cm, the maximum acceptance angle is taken to be $\pm$ 27° in the direction perpendicular to the Micromegas readout strips.

The SM2 module consists of four layers of active volumes and is trapezoidal in form in order to meet the shape of the NSW (Fig. 4.3a). The four active layers are labelled as the outer eta layer (EO), inner eta layer (EI), inner stereo layer (SI) and outer stereo layer (SO). The active surface area of the Micromegas module is about 2 m^2, which is covered by 3072 parallel readout strips per layer of pitch 0.425 mm. The eta layer strips run parallel to the trapezoidal frame's parallel sides. The number of a strip detecting a signal determines the accurate position of the signal in the direction perpendicular to the strips. The precision direction of the

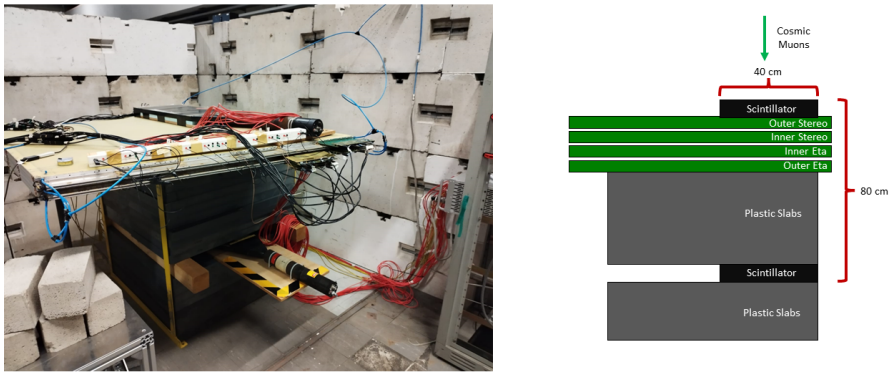

FIGURE 4.2: *Left*: Set-up for the cosmic muons measurements with the SM2 module placed in between the two scintillators which are used for triggers. *Right*: the corresponding schematic for the set-up. Only cosmic muons with angles $< \pm 27^{\circ}$ in the direction perpendicular to the strips triggering both the scintillators in coincidence are considered as an event.

module is thus defined as the direction perpendicular to the strips, while the non-precision direction refers to the direction along the strips.

Each strip measures 0.325 mm wide and the eta layers have a readout pitch of 0.425 mm while the stereo layer pitch is smaller at 0.42485 mm (Herrmann 2019). This is due to the stereo layers being oriented $\pm 1.5^{\circ}$ towards the eta-strips and 3 degrees towards each other, resulting in the aberrant width of the stereo pitch. This tilt in strips for the stereo layers allows for a coarse reconstruction along the non-precision direction (Fig. 4.3b).

4.3 Data Analysis

The aim of the analysis is to check the homogeneity of the efficiency of the Micromegas detector, in order to investigate whether the long-term irradiation of neutrons and gammas from the Am-Be source resulted in the deterioration of the detector performance. This majorly involves the ability of the detector layers to register the correct signal hit, enabling the analysis to accurately perform a track reconstruction.

Measurements were taken for differing anode voltage scans for the two gas mixtures. Each time a coincidence on the scintillators occured, an event was recorded

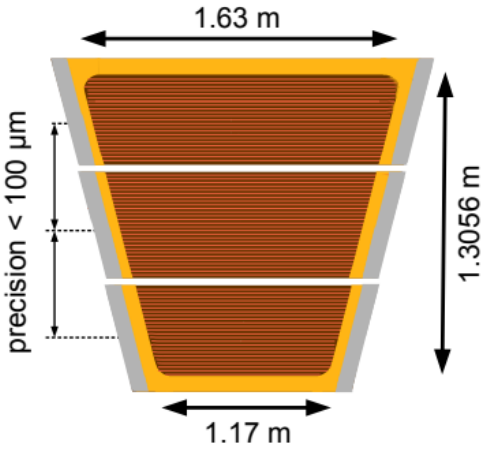

(a) Schematic of the size of the SM2 module. The readout anode is segmented into three PCBs which are glued precisely together. The brown area indicates the active region while the orange region indicates the inactive region. The grey area shows the connections to the electronics and cooling.

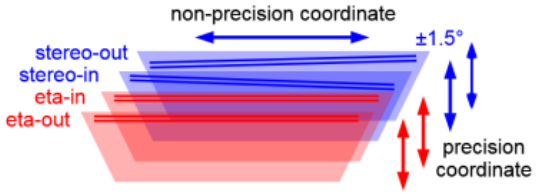

(b) Orientation of the strips in the eta and stereo layers. The stereo layers are tilted ± 1.5 ° towards the eta layers and 3 degrees towards each other. This allows for reconstruction with mm precision along the non-precision direction as well.

FIGURE 4.3: Fig. 4.3a shows the segmentation of the trapezoidal Micromegas module while Fig. 4.3b displays the alignment of the stereo layers to the eta layers. Figures adapted from (Herrmann 2019).

in the detector. The signals are collected in a timeframe of 600 ns using the APV25 front-end electronics that observes the collected charge from the readout strips for 24 time bins of 25 ns. This signal is processed and reconstructed to obtain clusters of responding neighbouring strips(Section 3.3). A muon travels in a straight direction and ideally creates only one cluster in each layer of the detector, enabling a clear linear track fitting, details of which are discussed in the following few subsections.

4.3.1 Hyper-cluster Formation

Since the stereo layers are tilted by 1.5° towards the eta layers, the position along the precision and non-precision direction can be reconstructed. The precision coordinate 'y', running perpendicular to the eta layer strips, is simply determined using (Alexopolous 2015)

$$y = \frac{v + u}{2 \cdot \cos(\alpha)} \tag{4.2}$$

where v and u are the positions of the charge-weighted centres of the clusters of the two stereo layers. Similarly, the non-precision coordinate 'x' is calculated using

$$x = \frac{v - u}{2 \cdot sin(\alpha)} \tag{4.3}$$

where $v - u$ is the difference in the charge-weighted center of the two clusters used and α is the tilt angle in radians. In order to use this method of determining the position of this virtual cluster, which is referred to as a hyper-cluster, it is implicitly assumed that both sets of read-out strips are located in the same plane (Flierl 2018). The z-axis position along the detectors of this hyper-cluster is fixed halfway between the two stereo layers on a plane for all hyper-clusters.

4.3.2 Track Reconstruction

The track is reconstructed for each layer iteratively, using the other layers for reference tracks. An example of the track reconstruction is given in Fig. 4.4. Tracks are constructed only if all the layers have at least one hit. The number of clusters created in each layer can be seen in Fig. 4.5. The charge-weighted mean cluster timing of all the clusters in the outer eta layer is depicted in Fig. 4.6. Similar to the centroid method (eq. 3.7), the time of all channels in the cluster is weighted with the channel charge and summed. The total charge of the cluster is divided by the sum to get the charge-averaged cluster time.

A first-order polynomial track is constructed using the clusters from the reference layers. The centroid method is applied for the position reconstruction of these clusters up to 5° angles; beyond that, the time-corrected charge-weighted position reconstruction method is used. If all the reference layers have exactly one cluster, the precision coordinate of the reconstructed hit from the reference tracks is compared to the closest hit position in the form of residuals which determine the spatial resolution of the detector. If the reference layers have multiple hits, only events with exactly one cluster in the investigated layer are taken and the reference track is chosen based on the cluster closest to the reconstructed hit of the track.

The angle of the incidence for the particle which is needed for the position reconstruction using the time-corrected charge-weighted method is estimated using the slope of the reconstructed track p_1.

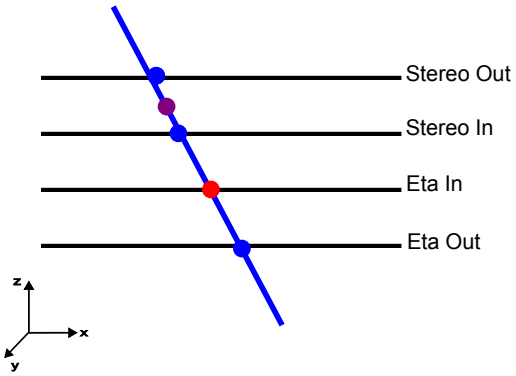

(a) Track reconstruction using the outer eta (in blue) and the hyper-cluster from the stereo layers (in purple) as reference clusters. The precision coordinate of the hyper-cluster is determined from the clusters of two stereo layers (in blue) using eq. 4.2 and lies in the middle of the two layers along the z-axis. The expected hit position in the investigated inner eta layer is denoted in red.

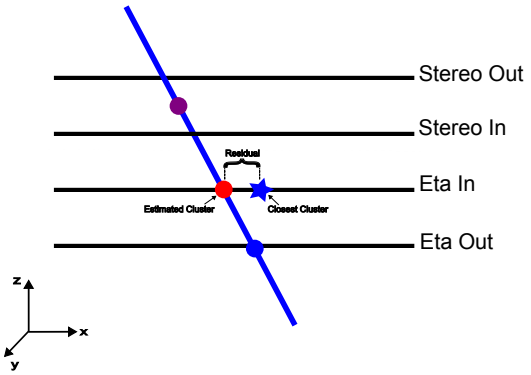

(b) The difference between the reconstructed hit (red circle) and the closest cluster in the inner eta layer (blue star) in the precision direction determines the residual of the probed layer (here, the inner eta layer).

FIGURE 4.4: Fig. 4.4a shows an example track reconstruction from the clusters of the reference layers (here, the outer eta and two stereo layers). Fig. 4.4b shows the expected hit position from the reconstructed track and the closest cluster found in the inner eta layer.

4.3.3 Residuals

Once the track has been reconstructed, the cluster in the investigated layer nearest to the position of the reference track is selected. The residual, or the distance between the measured cluster position x_{meas} and the reconstructed position of the reference track x_{ref}, is given by

$$\Delta x = x_{ref} - x_{meas} \tag{4.4}$$

The residual is retrieved for each event in this layer and recorded in a histogram that displays a Gaussian distribution with broadened tails. A fit using the sum of two Gaussian distributions is performed, one for the narrow core of the observed distribution and one for the broader tails such that

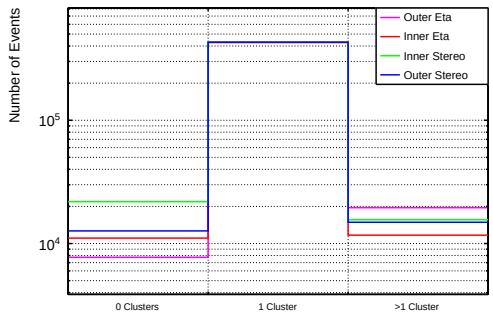

FIGURE 4.5: Plot of the number of clusters created in all four layers. This measurement was taken for the anode voltage set to 530 V in the ternary gas mixture of Ar:CO_2:iC_4H_{10} for 600,000 triggers. It can be seen that $\approx$75% of the time only single clusters are observed.

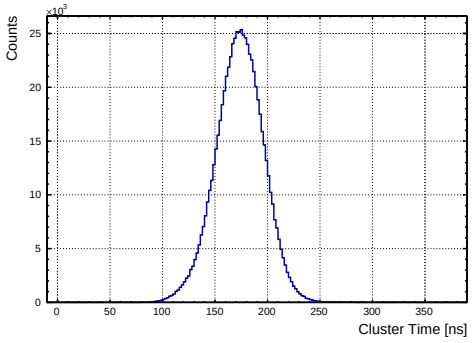

FIGURE 4.6: The charge-weighted mean cluster timing of all clusters in the outer eta layer has a distribution with a total width of 150 ns, which corresponds to 6 time bins. The uneven distribution around the peak is due to the angular spectrum of the cosmic muons accepted.

$$gauss_{double}(x) = gauss_{core}(x) + gauss_{tail}(x) \tag{4.5}$$

The width of the core Gaussian σ_{core} can be considered the resolution of the detector while the width of the tail Gaussian σ_{tail} physically represents the contributions from δ-electrons or multiple scattering of the lower energetic cosmic muons. The weighted residual σ_{weighted} of the detector is then estimated to be

$$\sigma_{weighted} = \frac{\sigma_{core} \int gauss_{core}(x) + \sigma_{tail} \int gauss_{tail}(x)}{\int gauss_{core}(x) + \int gauss_{tail}(x)} \tag{4.6}$$

The investigation of the inner eta layer, with the outer eta and stereo layers as the reference tracks, has the best residuals among all the layers since the reconstructed hit is interpolated and has a core residual of 139 µm as can be seen in Fig. 4.7. Since the measurements are performed with cosmic muons, it must be taken into account that the residuals are negatively affected by the angular distribution of the cosmic muons. Fig. 4.8 shows the residuals estimated versus the slope after applying the time-corrected charge-weighted position reconstruction. It must also be kept in mind that the muon spectrum of the cosmic muons allows for muons with substantially lower energy, implying an even greater susceptibility to multiple scattering. Using only high energetic muons entering at a known angle will produce better residuals with these detectors.

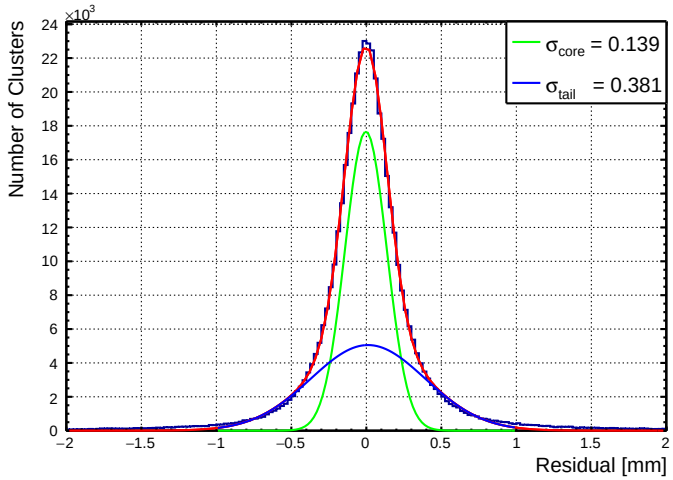

FIGURE 4.7: Residuals of the investigated inner eta layer clusters in comparison to the hit cluster in the precision direction. The function is fit to a double Gaussian with the core Gaussian having a residual of 139 μm.

The σ_{weighted} values as a function of voltage scans for both gas mixtures is given in Fig. 4.9. It is important to note that the tracking errors haven't been included in the estimation of these residuals. They can be large for tracks with big angles

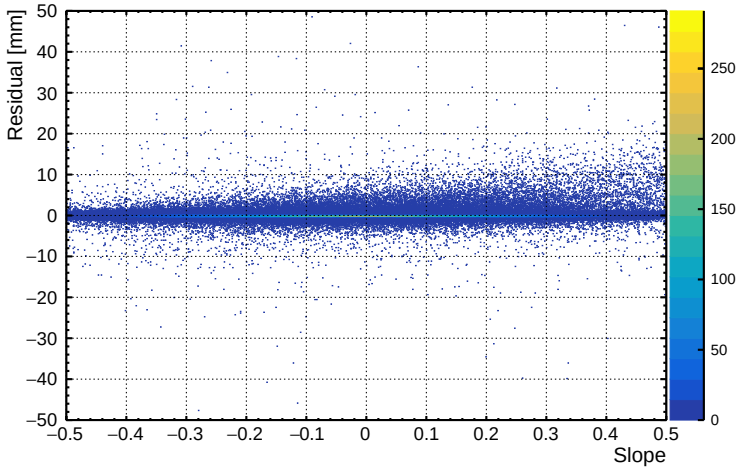

FIGURE 4.8: Residuals for the investigation of the inner eta layer vs. the slope of the reference track after the time corrected charge weighted position reconstruction is applied.

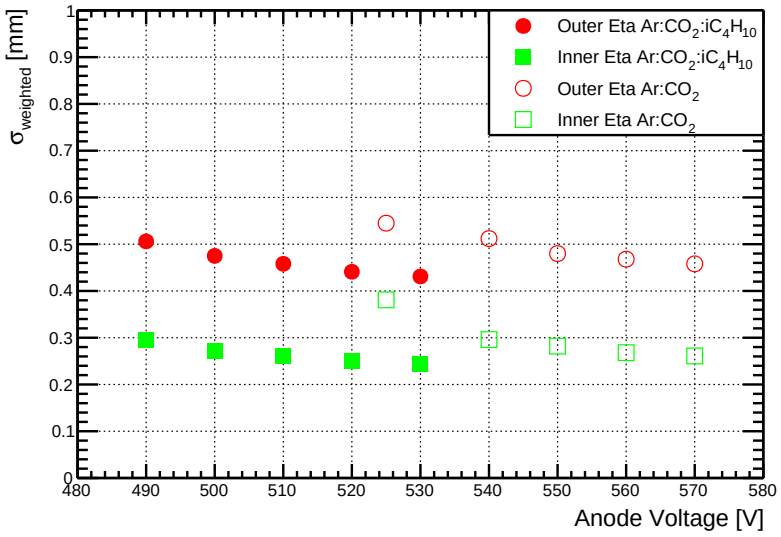

FIGURE 4.9: Weighted residuals of the eta layers as a function of different anode voltages. Residuals of the inner eta layers are significantly better due to the interpolation of the reference track for the determination of its residual.

since the clusters in the reference layers use the centroid position reconstruction method. This can be improved with the help of an external track created with two additional reference detectors, enabling the application of time-corrected charge-weighted position reconstruction for all the layers.

4.3.4 Pulse Height Measurements

The charge associated with each cluster is given in Fig. 4.10. The distinct Landau-shaped distribution due to the thin media, i.e. the width of the gas region, shows that the most probable value (MPV) of the charge is much lower than the mean value (see Section 2.1).

The most probable value of the fit is affected by the operating parameters, specifically the gas mixture and the amplification voltage used. Pulse height measurements for cosmic muons were taken at different amplification voltages under Ar:CO_2 and Ar:CO_2:iC_4H_{10} gas mixtures and plotted in Fig. 4.11. The MPV can be observed shifting to higher values with an increase in the amplification voltage, which results in higher gain during the Townsend avalanches. The corresponding equal gain for 570 V in Ar:CO_2 can be seen at $\sim$515 V. The real trend

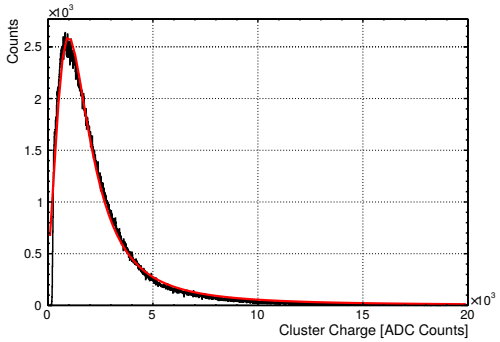

FIGURE 4.10: Landau distributed cluster charge in the inner eta layer for U_{anode}= 530 V in Ar:CO_2:iC_4H_{10}. The most probable value is taken as the cluster charge for this layer.

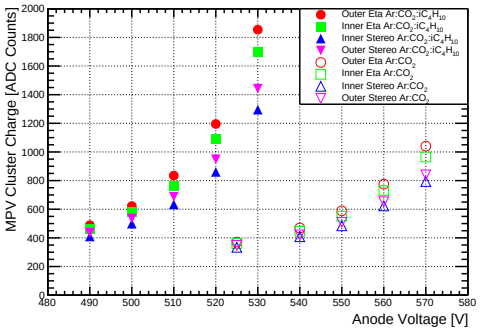

FIGURE 4.11: The most probable value of the pulse height for all the layers. The slight deviation in the pulse height for different layers at the same voltage can be attributed to production differences since the stereo and eta layers were manufactured by different companies (Herrmann 2019).

is also influenced by the surrounding environmental conditions, such as temperature, pressure and humidity. Since the manufacturing companies that produced the stereo and eta layers were different, some differences in the construction can be observed (Herrmann 2019). A decrease in the pulse height for the stereo layers is a direct influence of their higher pillar heights.

4.4 Efficiency of Cosmic Muon Tracking

The efficiency of each layer is determined from the residual fit given in Fig. 4.7. A layer is deemed efficient if a reconstructed cluster has an absolute residual below 5 mm. The number of efficient clusters is then divided by the total number of clusters found in the investigated layer. This is a common technique agreed upon by the Micromegas community for large area Micromegas detectors (Scholer 2021).

Fig. 4.12 shows the efficiency of the outer eta layer, which was the layer placed closest to the Am-Be source in the z-direction, in the precision and non-precision direction, at anode voltage set to 530 V for the isobutane gas mixture. The position of the centre of the source is indicated with a black marker; it can be seen that there is no decrease in the efficiency of the detector in the immediate vicinity of

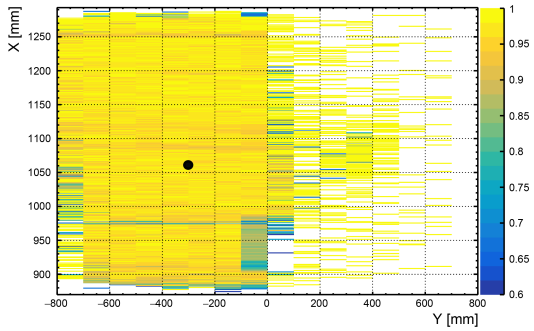

FIGURE 4.12: Efficiency of the outer eta layer with respect to the precision and non-precision coordinates. The centre of the neutron source is denoted with a black mark. The triangular shape of the weakly scintillating Plexiglas of the scintillator can be seen right of y=0.

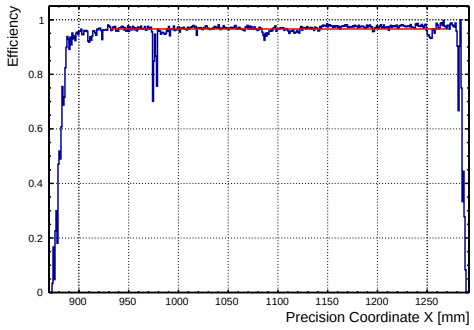

FIGURE 4.13: Fitted efficiency of the outer eta layer for the anode voltage 530 V in the ternary gas mixture of Ar:CO_2:iC_4H_{10}. The three observable dips are corresponding to the faulty APV25 electronics, as can be seen in Fig. 4.12 at the same strip numbers.

the black marker. A slight decrease along the strips between 1087 to 1142 mm is observed due to a single faulty APV25.

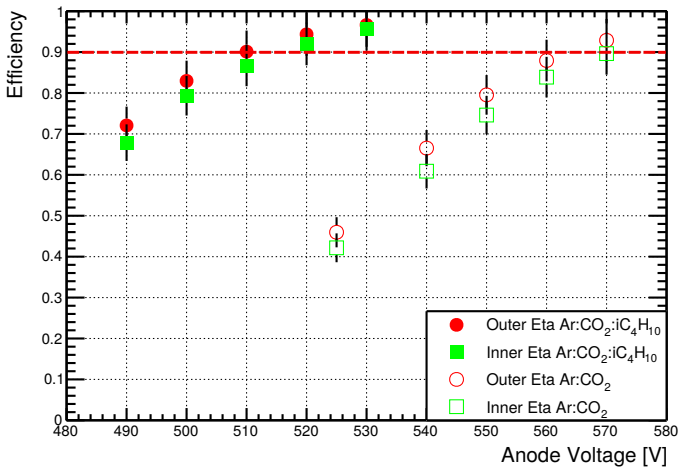

FIGURE 4.14: Efficiency scan as a function of the applied voltage on the strips. The plot shows that the efficiency is above 90% for all the eta layers at higher amplification voltages.

The fitted efficiency of each layer is estimated using a zero polynomial function

(see Fig. 4.13). These efficiencies are plotted as a function of different anode scans for both the eta layers for the two gas mixtures and can be seen in Fig. 4.14. The efficiency reached for the amplification voltage of 570 V in Ar:CO_2 is achieved with Ar:CO_2:iC_4H_{10} at an amplification voltage of 510 V. Efficiencies above 90% are the standard requirement for high rate capable detectors which is successfully met for higher amplification voltages for both gas mixtures. In conclusion, it can be established that the three years of high background irradiation show no deterioration in the performance of the detectors.

Chapter 5

Neutron Source Characterisation

5.1 Theoretical Principle and Motivation

The source used as background radiation for the Micromegas detector measurements is an Americium-Beryllium (Am-Be) neutron source having an activity of 10 GBq. The entire source is cylindrical in shape, measuring 19.4 mm long and 17.5 mm in diameter (Fig. 5.1). The active volume at the centre of the cylindrical source contains the Am-Be powder created by mixing powdered beryllium metal with an oxide of the alpha emitter. The active volume, which is 11.8 mm in length and 14 mm in diameter is housed in doubly-encapsulated stainless-steel layers whose endcaps are TIG (Tungsten Inert Gas) welded. The highly active source produces neutrons in the MeV energy range in a $^{9}\mathrm{Be}(\alpha,\mathrm{n})^{12}\mathrm{C}^{*}$ nuclear reaction given by

$$^{241}Am \rightarrow {}^{237}Np + \alpha + \gamma(59.54keV) \tag{5.1}$$

where α particles are emitted from the α decay of ^{241}Am, with a weak 59.54 $\approx$ 60 keV photon as a by-product in 35.9 % of the decays. The daughter ^{237}Np is a long-lived isotope with a half-life of over 2 million years. These α particles then react with the ^{9}Be to produce an excited $^{13}\mathrm{C}^{*}$ via $^{9}\mathrm{Be}(\alpha,n)^{12}C^{*}$ reaction

$$^{9}Be + \alpha \rightarrow {}^{13}C^{*} \tag{5.2}$$

where the compound nucleus emits a neutron with a highly excited ^{12}C which can be de-excited in several ways, out of which one of them is

$$^{13}C^{*} \rightarrow {}^{12}C + n + \gamma(4.438MeV) \tag{5.3}$$

which has an assumed branching ratio of 0.591 for the 4.438≈4.4 MeV photons to the number of fast neutrons produced (Croft 1989). The isotropic neutron yield of the source is $6 \cdot 10^4$ neutrons per second per GBq, with the intensity of the neutrons given in Fig. 6.8. The energies are usually in the range of 1-11 MeV with an average energy between 4 and 5 MeV.

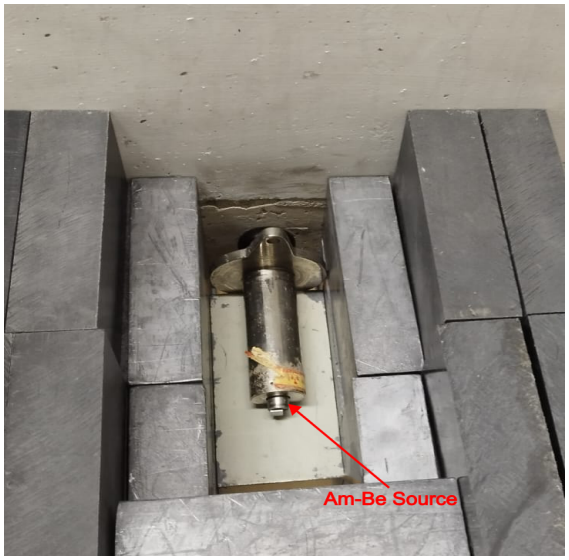

FIGURE 5.1: The Am-Be neutron source is visible here (blue), placed at the tip of the cylindrical case. The source is shielded from all sides with lead and borated plastic bricks seen here.

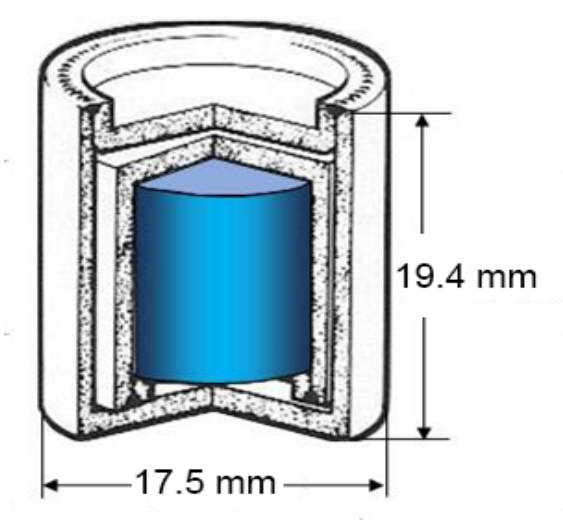

FIGURE 5.2: Schematic drawing of the Am-Be source doubly encapsulated in stainless steel layers. Image adapted from (Bjørnstad 2021).

Thus for the Am-Be source, 10 GBq α decays gives an activity $A_{neutron} \approx 6 \cdot 10^5$ neutrons per second and $A_{4.4MeV} \approx 3.5 \cdot 10^5$ 4.4 MeV gammas per second. From the α decay of ^{241}Am, we also get $A_{60keV} \approx 3.6 \cdot 10^9$ 60 keV photons per second. As mentioned before, a characterisation study is necessary to fully understand the gamma intensity distribution that the detector actually sees after absorption from the surrounding materials, especially for the 60 keV photons. The objective of this part of the thesis is to clarify the characteristics of the neutron source used by disentangling the contributions of the photons and neutrons that undergo various interaction processes with the detector material. The estimated relative intensity ratio R of the weak 60 keV photons to the 4.4 MeV gammas is given by

$$R = \frac{A_{60keV} \cdot I_{Be} \cdot I_{Housing}}{A_{4.4MeV}} \tag{5.4}$$

The total intensity of 60 keV photons taking into account the absorption in the powdered Beryllium with I_{Be} and after passing through the encapsulated housing is given by $I_{Housing}$. To confirm the intensity ratio between the 60 keV photons and the 4.4 MeV gammas, a Germanium detector is used to obtain the gamma intensity distribution of the Am-Be source. Once this factor is obtained, it is implemented in a Geant4 simulation to determine their behaviour and disentangle the contributions of the weak 60 keV photons as well as the stronger MeV gammas and neutrons.

5.2 Germanium Detector

In order to understand the actual intensity distribution of the Am-Be source, a High Purity Germanium (HPGe) detector was used to perform the gamma spectroscopy of the source. Germanium detectors have excellent resolutions at low energies due to their small average energy of 2.9 eV required to create an electron-hole pair and having a band gap of 0.67 eV. Germanium detectors have a high linear attenuation coefficient due to their large atomic number, making them ideal for detecting photons in the MeV energy range.

The limitation of semiconductor detectors of normal purity is the width of their sensitive region due to their dependence on the applied bias voltage such that (Knoll 1979)

$$d = \sqrt{\frac{2\epsilon V}{eN}} \tag{5.5}$$

where d is the thickness of the depletion region, V is the applied reverse bias voltage, with ϵ being the dielectric constant and N being the net impurity concentration. Increasing the voltage up to the breakdown level results in a maximum depletion thickness of 2-3 mm (Knoll 1979). A possible way to achieve the required thickness to completely absorb high energy photons is by increasing the purity of the detectors. Hence, these HPGe detectors, having a sensitive volume in cm ranges, can be used to determine the intensity of the high 4.4 MeV photons and the low 60 keV photons irradiated by the source.

5.2.1 Functional Principle

Fig. 5.3 depicts a schematic of an HPGe detector. Germanium detectors are semiconductor diodes having a p-i-n structure, where ionising radiation enters the Germanium crystal i.e. the sensitive volume of the detector, and interacts with

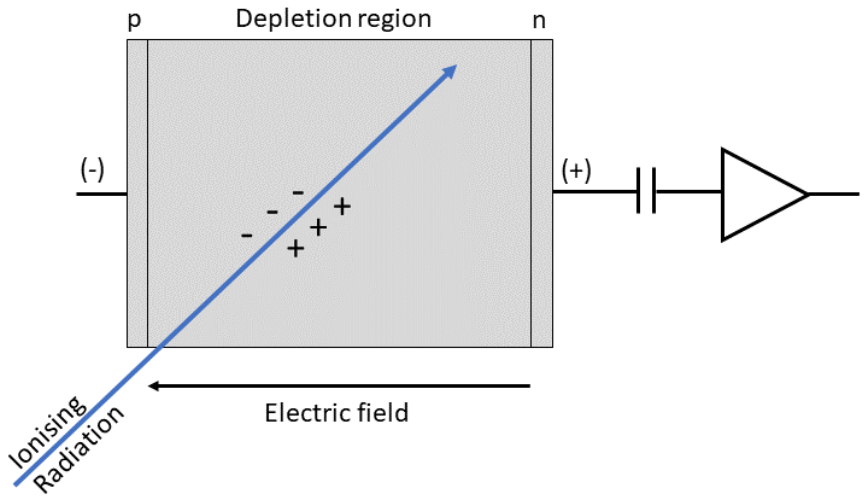

FIGURE 5.3: Schematic illustration of a photon passing through an HPGe detector. When photons interact with the substance within the detector's depleted zone, charge carriers are created and carried to the P and N electrodes by the electric field. This charge is then converted into a voltage pulse using a charge-sensitive amplifier.

the semiconductor material producing electron-ion pairs. Under the influence of an electric field, these electron-hole pairs migrate to the electrodes. An integral charge-sensitive preamplifier followed by a shaping amplifier converts this charge, which is proportional to the energy deposited in the detector by the incoming photon, into a voltage pulse signal.

Since Germanium has a relatively small band gap ($E_{gap} = 0.67$ eV), thermal excitations due to impurities and lattice structure deformities dominate at room temperatures, creating high detector noise. These detectors thus need to be cooled to reduce the thermal excitations to an acceptable level and this is done by operating the detectors at very low temperatures using liquid nitrogen ($\approx -196^{\circ}C$).

The voltage pulses are fed to an Amptek MCA8000D Multi-Channel Analyser (MCA)[3], which uses a fast ADC to convert the analogue signals and stores the information about the pulse amplitude in different channels. This is known as the Pulse-Height Analysis (PHA) mode. The gamma spectrum is a histogram of these

[3] https://www.amptek.com/-/media/ametekamptek/documents/resources/products/user-manuals/mca8000d-user-manual-b1.pdf?la=en&revision=75b93881-a2e4-4d92-9d84-0d67b5d34614

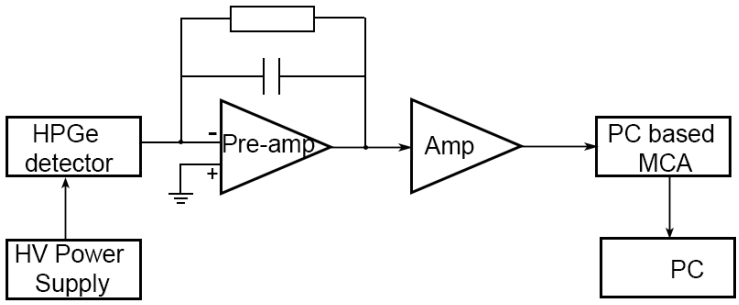

FIGURE 5.4: Circuit diagram of the HPGe detector system used. An integral charge-sensitive preamplifier followed by a shaping amplifier converts the charge created in the detector, which is proportional to the energy deposited in the detector by the incoming photon, into a voltage pulse. This pulse is fed to an MCA which converts the analogue signal and stores the information about the pulse amplitude.

pulses, with the height of the channel corresponding to the number of pulses in a certain amplitude range. Once the data is stored in a histogram, it is sent to a computer via USB or Ethernet.

5.2.2 Detector Calibration and Efficiency Determination with Multiple Sources

The HPGe detector coupled with an MCA was first calibrated with the energy of known sources before using it to analyse the gamma spectrum of an unknown source. For this purpose, the following radioactive isotopes of known activity and gamma spectra are used: ^{137}Cs, ^{60}Co, ^{241}Am and ^{152}Eu. The detector set-up for the calibration procedure is shown in Fig. 5.5.

Measurements for each source were taken for a duration of 300 seconds and the resulting spectra for one of the sources, ^{137}Cs, can be seen in Fig. 5.6 along with its associated decay scheme in Fig. 5.7. The gamma spectrum clearly shows the distinct photopeak from the 662 keV γ line of ^{137}Cs at channel 500. Using these photopeaks from all four calibration sources, the linear relationship between the channel number from the detector output and the corresponding deposited energy was found such that

$$E = 1.278 \cdot [ChannelNo.] + 10.42 \tag{5.6}$$

as can be seen in Fig. 5.8. Once the detector has been calibrated to this function, the efficiency over different energies must be determined. The counting efficiency

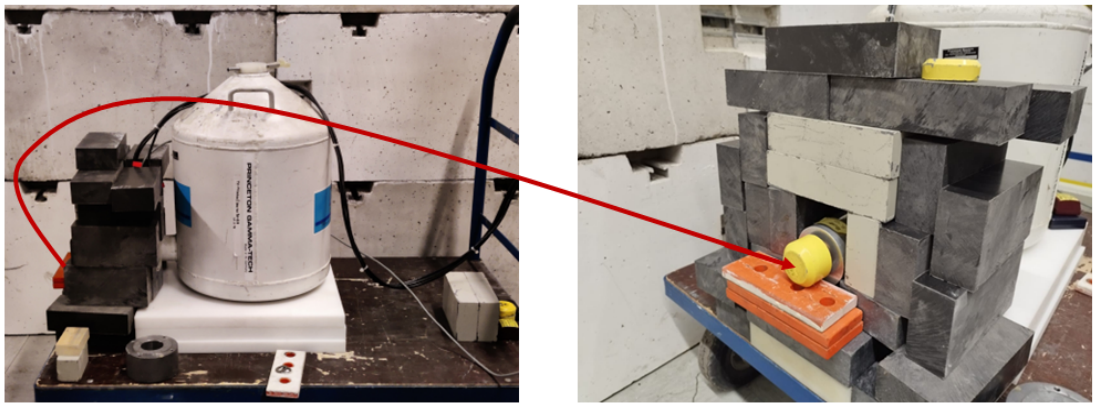

FIGURE 5.5: Set-up for the energy calibration of the HPGe detector. *Left*: Side view of the detector. The detector is attached to the cryogenic storage dewar containing liquid nitrogen for cooling. *Right*: Front view of the detector with one of the calibration sources placed right in front of the detector cap. Plastic and lead shielding is placed on the sides of the sensitive region of the detector to reduce background effects.

ϵ of the full energy peak is described by the following equation:

$$\epsilon = \frac{4\pi \cdot N}{A_s \cdot I_\gamma \cdot \Omega \cdot t} \tag{5.7}$$

where A_s is the activity of the source in Bq, I_γ is the gamma yield (Appendix A), Ω is the solid angle and t is the measurement duration in seconds. The value of N is determined by fitting a Gaussian distribution to the full energy peak. An example fit for the 122 keV gamma from the ^{152}Eu source is given in Fig. 5.9. These efficiencies measured require a suitable functional fitting and several such fitting functions are proposed in the literature (Gray and Ahmad 1985). The fitting parameters of these functions are usually non-linear and initial estimations are required to obtain the parameter values. The efficiency values are plotted in Fig. 5.10, where the full peak energy efficiency curve of the detector is estimated by fitting a polynomial function of the fourth order given by

$$\varepsilon = \frac{[p0] + [p1] \cdot (\ln E) + [p2] \cdot (\ln E)^2 + [p3] \cdot (\ln E)^3 + [p4] \cdot (\ln E)^4}{E} \tag{5.8}$$

where E is the photon energy. This function was chosen since it was suggested in the above literature and was found to give satisfactory results over the energy

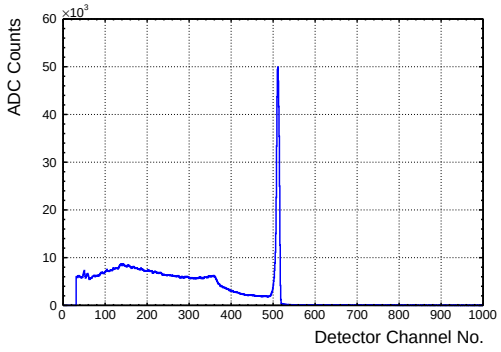

FIGURE 5.6: Gamma spectrum of ^{137}Cs with an activity 189 kBq. The Compton continuum of the 662 keV gammas can be seen here followed by the Compton edge at channel 360 before the distinct photopeak at channel number 500.

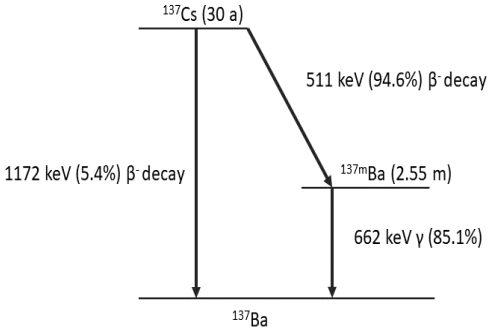

FIGURE 5.7: Associated Decay Scheme of ^{137}Cs. 85.1% of the time ^{137}Cs produces 662 keV gammas after beta decay.

range of up to 5000 keV.The parameters of this polynomial are given in Table 5.1.

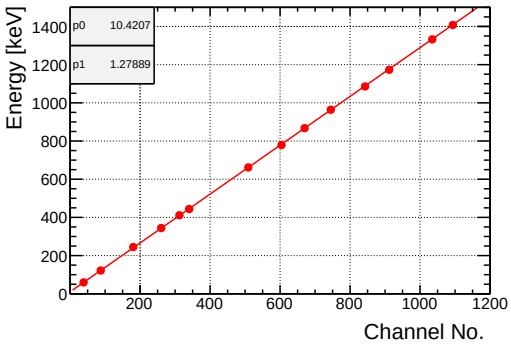

FIGURE 5.8: Linear relation between Channel No. and deposited energy required to calibrate the HPGe detector fit using a polynomial of the first order.

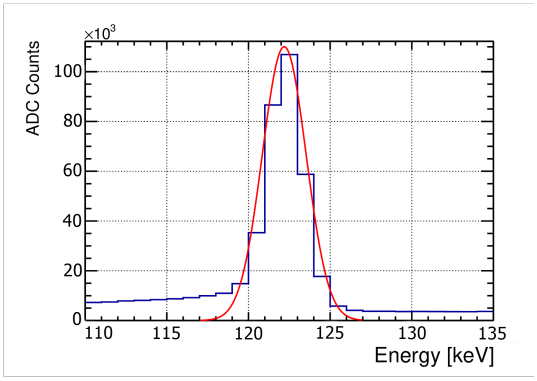

FIGURE 5.9: Gaussian fit to the full energy peak of the 122 keV gamma of ^{152}Eu.

5.2.3 Am-Be Source Gamma Spectrum

After the calibration of the HPGe detector, measurements with the neutron source were taken for $t = 3600$ s. The detector set-up, shown in Fig. 5.11, was changed for this measurement, keeping the source at a distance R $\approx$ 2 m from the detector due

Parameter List	
p0	-283.016 ±3.00827
p1	212.114 ±1.68583
p2	-91.3008 ±0.24626
p3	-2.31417 ±0.03503
p4	-2.80645 ±0.01214

TABLE 5.1: Parameters of the fourth order in ln(E) polynomial fit given in eq. 5.8 to the measured efficiencies for the full energy peaks of the calibration sources.

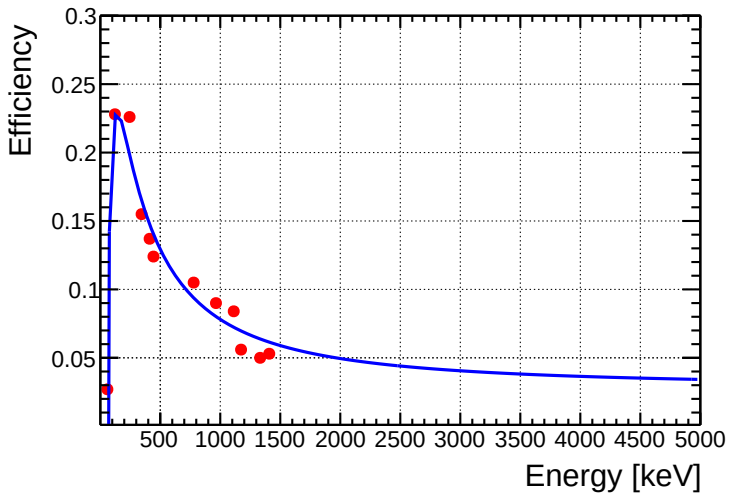

FIGURE 5.10: Full energy peak efficiency curve for all the photopeaks from the calibration sources used.

to its high activity. A lead collimator having an inner diameter $\varnothing \approx 50$ mm is used to reduce edge effects (Fig. 5.12). The solid angle of acceptance for small angles can be determined by $\Omega \approx A/R^2$ where A is the inner area of the collimator. For this set-up, the solid angle has been calculated to be $6.06 \cdot 10^{-4}$ steradians.

The resulting calibrated gamma spectrum can be seen in Fig. 5.13 for the 60 keV gammas, and with a zoomed-in look at the 4.4 MeV energy region in Fig. 5.14. The photopeak of the 60 keV gammas can be distinctly seen since this is the dominating interaction for photons in this energy range, as discussed in Section 2.2. Along with the 60 keV photon, the 100 keV photopeak of the ^{241}Am decay can be seen, which has an intensity of $1.9 \cdot 10^{-4}$. As a first test of the efficiency fit, the theoretical ratio versus the measured ratio of the two energies can be estimated. Assuming

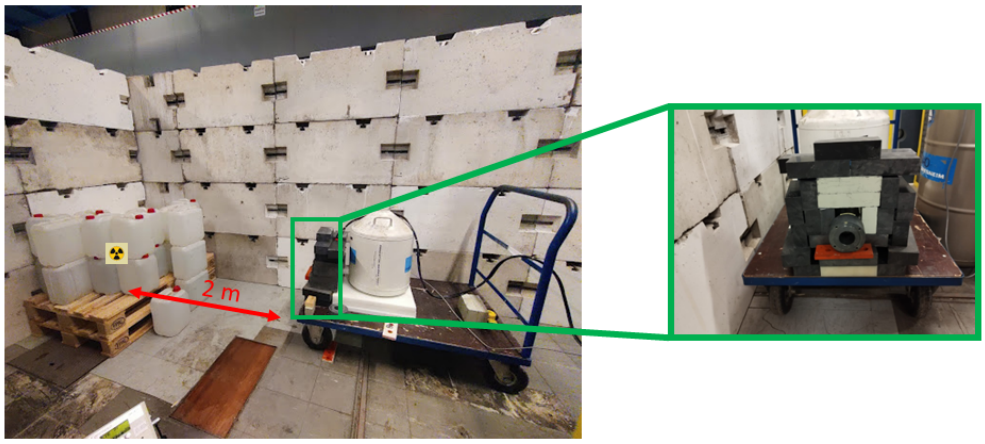

FIGURE 5.11: HPGe Detector set-up for the Am-Be source, kept at a distance of 2 m away, with lead, water and plastic shielding in all directions except the active area. A lead collimator of $\varnothing \approx 50$ mm is placed in front of the detector cap to reduce edge effects.

the photoabsorption probabilities of the two energies in Germanium have negligible differences, the theoretical ratio can be taken as $R_{theo} = I_{60keV}/I_{100keV}$. This value is estimated to be ≈1900. For the measured ratio, the full energy peak counts of both energies are fit to a Gaussian. The integral of the Gaussian and the relative efficiency between the two energies is taken from the polynomial function in eq. 5.8 such that

$$R_{meas} = \frac{N_{60keV} \cdot \epsilon_{100keV}}{N_{100keV} \cdot \epsilon_{60keV}} \tag{5.9}$$

The estimated ratio R_{meas} using the measured values, accounting for the efficiency is then calculated to be ≈1300 ± 8.057, which is a good first approximation and validates the efficiency fit used. The expected number of photons seen by the detector can be calculated using eq. 5.7 and is found to be $\approx 2 \cdot 10^7$ while the measured count $\approx 1.1 \cdot 10^7 \pm 2.3 \cdot 10^4$, which shows that there is no saturation of the detector.

For the 4.4 MeV gammas, there are three main contributing interactions: photoeffect, Compton effect and pair production. Along with the full energy peak at 4.4 MeV which includes the contribution from mainly pair production and a negligible contribution from photoeffect, the two peaks of the single and double escape peak from the pair production can also be seen (Section 2.2.3). The contribution from the interaction of photons via pair production will be the total sum of the full energy peak as well as the single and double escape peaks. In between the single escape peak and the photopeak, the Compton edge of the 4.4 MeV gamma can also be distinguished, placed ≈ 200 keV below the full energy peak. The count

ratio of the pair production contribution of 4.4 MeV gammas to the full energy peak of the 60 keV photons, accounting for the relative efficiency between the two energies from the efficiency fit. The efficiency of the detector is extrapolated for the 4.4 MeV gammas.

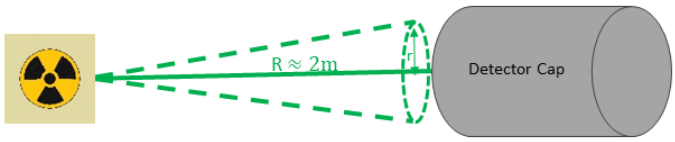

FIGURE 5.12: Schematic of the detector set-up for the Am-Be source. Here, R is the distance between the source and the detector and r≈ 25 mm is the inner radius of the collimator.

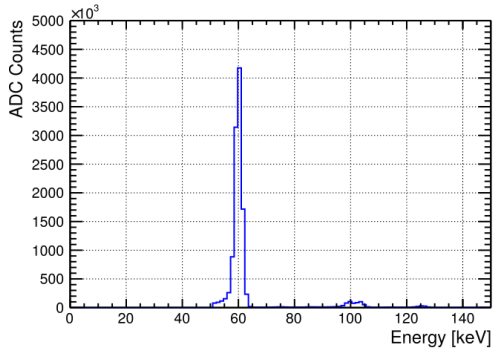

FIGURE 5.13: Gamma Spectrum of the 10 GBq Am-Be source in the lower energy range. The distinct photopeak of the 60 keV photon with a branching ratio 35.9% is visible, along with the 100 keV peak, which has a small branching ratio of 0.019%. The full gamma spectrum is given in Appendix A.

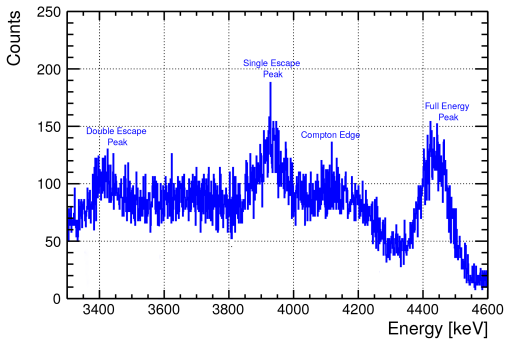

FIGURE 5.14: Gamma Spectrum of Am-Be source in the MeV energy range, with the full energy peak of 4.4 MeV gammas along with the single and double escape peaks. The Compton edge can also be distinguished here, just before the photopeak.

The photoabsorption probability P_{60keV} for 60 keV photons and the pair production probability $P_{4.4MeV}$ for 4.4 MeV gammas in Germanium are used to determine the total number of photons entering the detector (see Appendix B). Unfortunately, since the dimensions of the crystal are unknown, an assumption of 100

mm thick Germanium is considered for the calculation of this value. After the relative efficiency of the detector and the interaction probabilities of both energies are taken into account, the total intensity ratio R of the two energies can then be determined to be

$$R = \frac{N_{60keV}}{P_{60keV}} \cdot \frac{P_{4.4MeV}}{N_{4.4MeV}} \cdot \varepsilon_{rel} \tag{5.10}$$

Plugging in all the values (see Table 5.2), the total intensity ratio of the two photon energies is calculated to be ≈ 450. This factor is implemented while estimating the final contributions from these photon energies with a Geant4 simulation as described in the next chapter.

Ratio Values	
N_{60keV}	$1.1{\cdot}10^{7}$ $\pm 2.3{\cdot}10^{4}$
$N_{4.4MeV}$	$7.98{\cdot}10^{3}$ $\pm 1.96{\cdot}10^{2}$
P_{60keV}	0.85
$P_{4.4MeV}$	0.20
ε_{rel}	1.39 $\pm 3{\cdot}10^{-}4$

TABLE 5.2: Values used for the estimation of ratio R between the total number of 60 keV photons and 4.4 MeV gammas.[4]

[4]The absorption probabilities of both energies in 100 mm of Ge are taken from the XCOM database (Berger M.J. 2010) to determine the total number of photons entering the detector.

Chapter 6

Simulation of Source Interaction in Detector

6.1 Geant4 Simulation

The Geant4 toolkit by CERN is a freely available software package extensively used in high-energy physics to simulate the interaction of traversing particles with matter with high accuracy and provides us with the functionality of selecting physics processes such as hadronic, electromagnetic and optical processes over a wide energy range (Agostinelli et al. 2003). For this thesis, a Geant4 simulation was used to simulate all relevant interactions of the particles from the Am-Be source passing through the different materials of the Micromegas detector and obtain the total number of electrons in the drift region.

During the irradiation period of the Micromegas detector (see section 4.1), the neutron source was placed 25 mm away from the detector to accommodate 5 lead slabs of thickness 5 mm. The current drawn from the detector was measured for the incrementing thickness of lead. These current measurements are compared to the simulation results in section 6.2.

6.1.1 Simulation Set-Up

The physics list used for this simulation is QGSP-BERT-HP, an official physics list from Geant4 which implements the Quark-Gluon String model (QGSP) and Bertini Cascade (BERT) and is chosen based on its suitability for high energy physics containing standard electromagnetic processes as well as a high precision neutron model for neutrons with energy less than 20 MeV (HP)[5]. The geometry of

[5] https://geant4-userdoc.web.cern.ch/UsersGuides/ForApplicationDeveloper/fo/BookForApplicationDevelopers.pdf

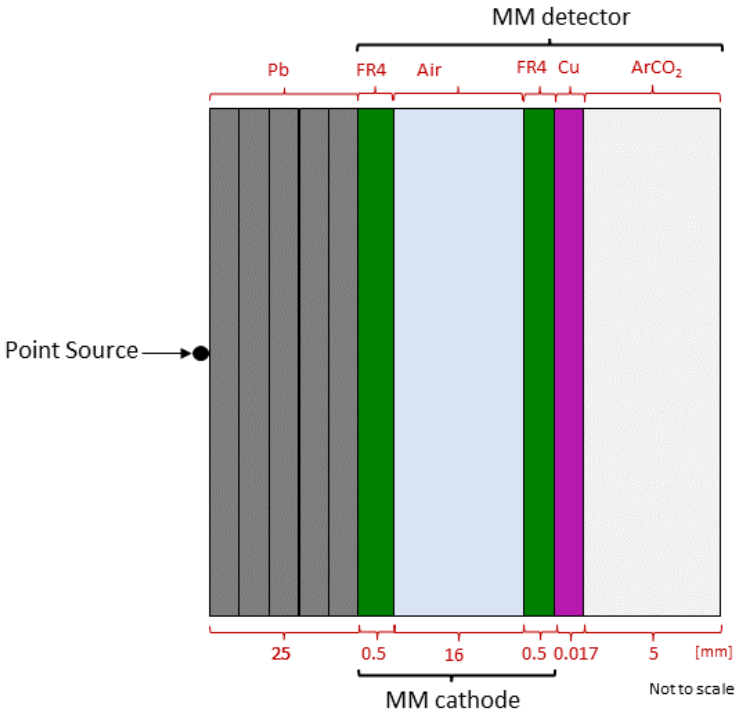

FIGURE 6.1: Schematic of the geometry set-up used for the simulation; here all 5 mm slabs of lead are placed in front of the detector cathode.

the set-up in the simulation, as seen in Fig. 6.1, is set according to the dimensions of the Micromegas detector with the gas mixture used in the simulation being Ar : CO_2 in the ratio 93 : 7 vol%. Lead slabs of thickness 5 mm each are placed in front of the detector in order to investigate the photon attenuation for increasing thickness (see Section 6.1.2).

The simulation is run for each particle for six iterations of 200,000 events, with the first iteration having 25 mm of air placed in front of the detector instead of lead shielding. Each iteration thereafter replaces the air with slabs of lead in increments of 5 mm thickness. A point source emitting particles isotropically in 4π is placed immediately in front of the detector, which means that roughly only 100,000 events actually enter the geometrical set-up.

The simulation generates primary particles according to the user-defined energies (in this case: 60 keV photons, 4.4 MeV photons and 1-10 MeV neutrons) that traverse the detector and counts the total number of primary electrons created by the

incoming particle in different materials of the detector via various interaction processes discussed in section 2.2 and 2.3. Because of the drift voltage applied in the real detector measurements, all primary electrons created in Ar : CO_2 or reaching the gas mixture from the other materials are presumed to reach the amplification region. Since the electric field is not applied in the simulation, this assumption must be made in order to obtain an estimate comparable to the true measurement.

It is important to note that in the context of the simulation, primary electrons refer to the electrons created from the first interaction of the incoming particle with the detector material, while the secondary electrons refer to the electrons created from either the ionisation by primary electrons or the secondary interactions of the radiating particle. Both these primary and secondary electrons are considered for the total number of electrons that enter the amplification region.

The simulation results for the number of extracted electrons are used to compare the current drawn from the Micromegas detector for a similar geometry set-up, with lead slabs of 5 mm, since the current must be proportional to the number of electrons in the drift region.

6.1.2 Photon Conversion and Transmission

To disentangle the contributions of the 60 keV photons of the ^{241}Am α-decay from the MeV photons and neutrons, lead slabs are placed in front of the detector to absorb them. Lead is a good attenuator of photons due to its high density and the attenuation is described by the Beer-Lambert law (Kleinknecht 1998)

$$I(x) = I_o \cdot \exp\left(-\frac{\mu}{\rho} \cdot \rho \cdot x\right), \tag{6.1}$$

where I_o is the incident intensity, ρ is the mass density, and x is the thickness of the material the incoming particle is passing through. μ/ρ is the attenuation coefficient of the photon in a given material such that

$$\frac{\mu}{\rho} = \sigma \cdot \frac{N_A}{M} \tag{6.2}$$

where σ is the absorption cross section, N_A is Avogadro's number and M is the molar mass. Fig. 6.2 shows the intensity of the 60 keV and the 4.4 MeV gammas after attenuation for varying lead thicknesses. We see that most of the 60 keV photons get completely attenuated within 1 mm of lead. In comparison, the intensity for the 4.4 MeV photons drops by only 3% in the same thickness.

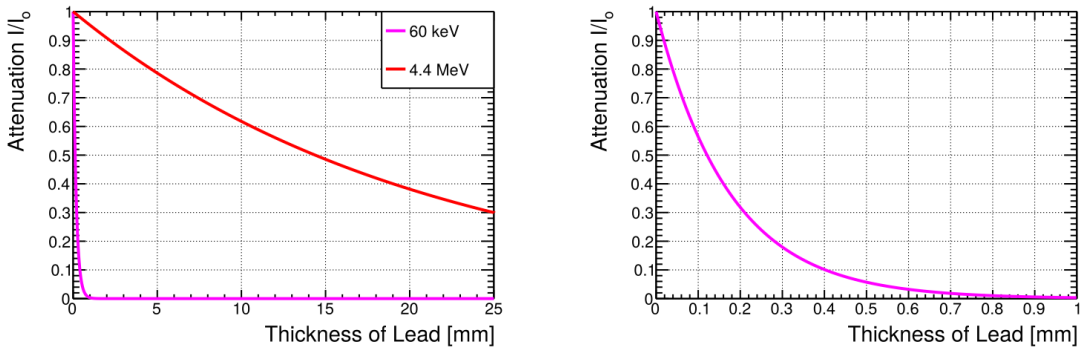

(a) Relative intensity of 60 keV and 4.4 MeV photons over 25 mm of lead.

(b) Attenuation of 60 keV photons over 1 mm of lead

FIGURE 6.2: Fig. 6.2a shows the attenuation plot of different photon energies decreasing exponentially over the increasing thickness of lead. Fig. 6.2b is zoomed in over a thickness range of 1 mm for the 60 keV photons. The intensity of the 60 keV photons reduces close to zero after passing through 1 mm of lead.

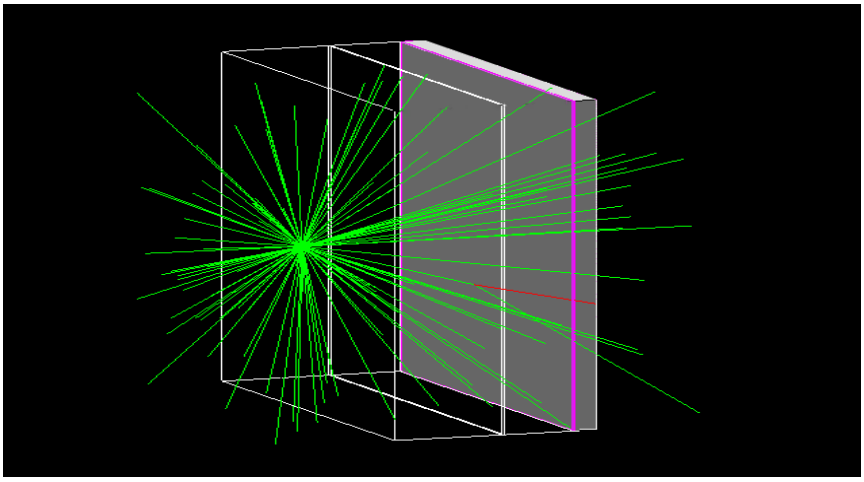

FIGURE 6.3: 100 simulated events for a point source emitting 4.4 MeV gammas with the magenta frame representing the copper layer and the grey solid box representing the Ar:CO_2 drift region. The green lines indicate the gammas while the red ones indicate the electrons. The electron tracks are not visible due to their small trajectories. The single electron track visible was produced via Compton scattering; the change in the angle of the photon is obvious.

Fig. 6.3 shows the visualisation of an exemplary simulation, consisting of 100 events, of the set-up and the particle trajectories for a point source emitting 4.4 MeV gammas isotropically in 4π, placed immediately before the detector set-up,

without any lead slabs. Most of the electron tracks created for 100 simulated events in the example cannot be seen in this figure due to their small trajectory, getting further ionised or recombined in the gas layer. In reality, this recombination will be prevented with an electric field in the drift region, hence why the assumption in Section 6.1.1 is important for the simulation and all the electrons created in the drift region are counted.

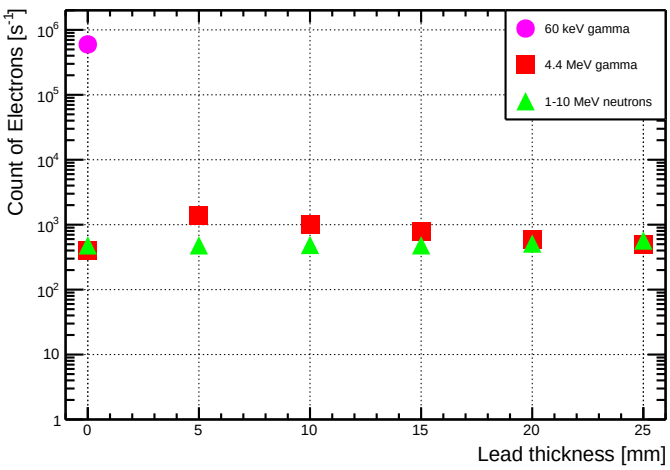

FIGURE 6.4: Plot describing the number of primary and secondary electrons, created by photons and neutrons emitted from the Am-Be source, reaching the drift region of the detector using Geant4 simulation.

The simulation results for the total number of electrons created in gas or reaching the gas in the simulated geometry for the incrementing thickness of lead are shown in Fig. 6.4 for all three irradiating particles, normalised to $6{\cdot}10^4$ neutrons, which have been weighted to their intensity distribution for the Am-Be source (see Section 6.1.3). As expected, the contribution from the 60 keV photons is completely attenuated after just 5 mm of lead. The high number of electrons from the 60 keV photons for the simulation with no lead also takes into account the normalisation factor R obtained using eq. 5.2.3 in the previous chapter.

For a gas mixture of Ar:CO_2 of 93:7% vol, the energy required to make an electron-ion pair is estimated to be $\approx$ 26.4 eV (Flierl 2018). This can be used to estimate the number of primary electrons that are created in the drift region. When a 60 keV photon passes through the detector, it interacts via photoeffect and produces photoelectrons in the energy of $\approx$50 keV, due to the k-edge of copper and argon which are 8.9 keV and 3.2 keV respectively. The mean number of primary electrons is calculated to be $\approx$ 150 since the mean energy loss in Argon for 50 keV electrons is

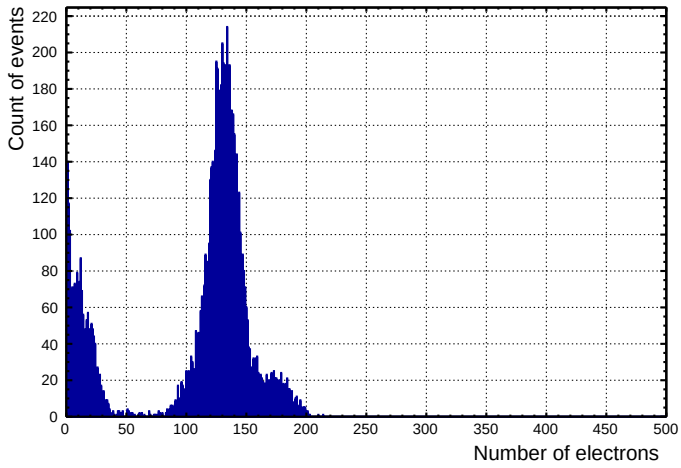

FIGURE 6.5: The number of primary electrons that are created by the 60 keV photons in the drift region for a gas mixture of Ar:CO_2 in 93:7% vol. The "Gaussian" peak at ≈130 is due to the 60 keV photon getting absorbed in Argon after 5 mm and emitting ≈50 keV electrons that go on to ionise more than 130 electrons. The lower contributions can be attributed to the low-energy electrons created.

7.5762 keV/cm. Fig. 6.5 shows the number of primary electrons created per event for 60 keV photons in the simulation. The "Gaussian" peak at ≈130 can be seen due to the 50 keV photoelectron traversing through 5 mm of argon. The higher contributions can be attributed to the Auger electrons created due to the k-shell electron being kicked out. [6]

Focusing on the 4.4 MeV contribution (Fig.6.4), a rise in the total number of electrons from zero to 5 mm of lead can be seen. This can be attributed to the multiple Compton scattering that they undergo in the lead, reducing the energy of the photons before they reach the copper layer. These lower energy photons have an increased cross-section in copper compared to the 4.4 MeV photons, resulting in a greater number of electrons reaching the drift region. Fig. 6.6 shows the position of the creation of electrons that are reaching this drift region for two simulations: with no lead and 5 mm of lead. For the simulation with lead, the majority of contributions come from the electrons created in gas and copper but a few high energetic electrons created in lead manage to reach the drift region as well. The contribution from the 4.4 MeV gammas then eventually decreases exponentially with increasing lead thickness due to absorption.

[6] All the ionisation energies mentioned (Ar, Cu) have been taken from (BEARDEN and BURR 1967).

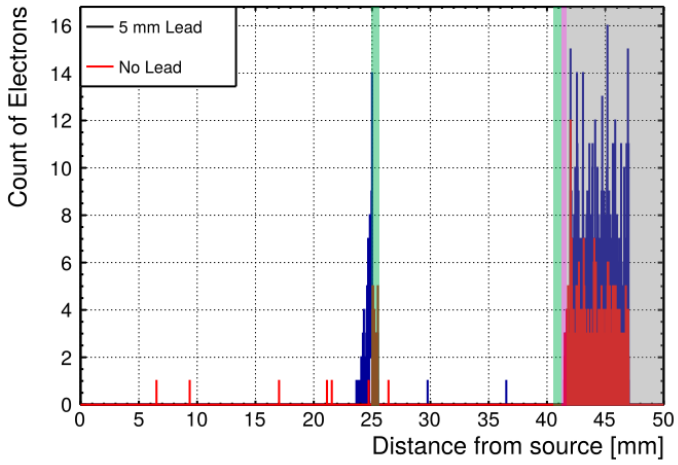

FIGURE 6.6: Position of all electrons created that reach the gas in no lead (red) and 5 mm lead (blue) for 4.4 MeV gammas. The grey box indicates the drift region while the magenta and green boxes signify copper and FR4 respectively. The electrons created in lead between x=20 to x=23 mm do not reach the drift region and get absorbed in the lead.

6.1.3 Neutron Conversion and Transmission

A similar simulation with neutrons in the energy range of $1 - 10$ MeV as incoming particles is performed with the same geometry. An example simulation visualisation of 100 simulated events of 5 MeV neutrons can be seen in Fig. 6.7. Since lead is not a good absorber of fast neutrons, the number of electrons reaching the drift region stays almost constant with the varying thickness of lead, which can be seen in Fig. 6.9. The results in this plot have been normalised to the nearest whole number with respect to the neutron intensity distribution of the Am-Be source given in Fig. 6.8.

These fast neutrons have a small interaction cross section due to their high energy, which is the reason why most of them leave the detector set-up with minimal interactions. The neutrons undergo scattering mainly in the gas itself and most of the electrons extracted are the ones created in gas. However, on placing the lead in front of the detector, some electrons created in the lead manage to reach the drift region (Fig. 6.10). The figure shows that only the electrons created towards the end of the lead, i.e. after x=24 mm manage to reach the drift region. The rest of the electrons are absorbed in lead.

[7] https://www.nrc.gov/docs/ML1122/ML11229A704.pdf

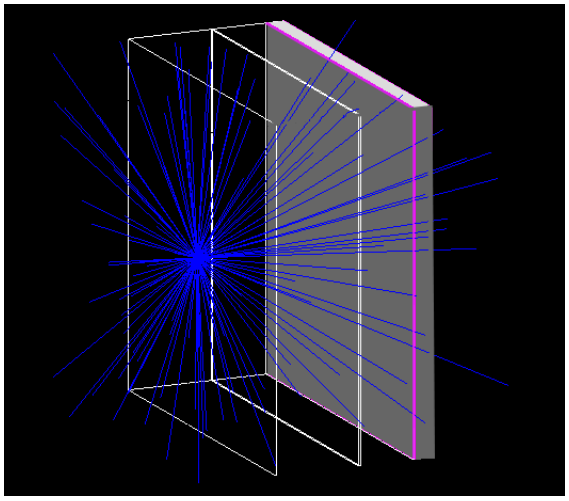

FIGURE 6.7: Trajectories of 5 MeV neutrons traversing the detector without any Lead slabs placed in front of it. Most of the neutrons leave the detector without any interactions.

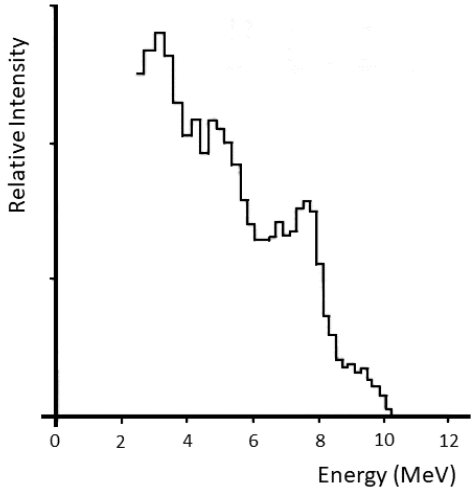

FIGURE 6.8: Intensity distribution of Am-Be source from 1-10 MeV, adapted from NRC [7]. The mean energy E is at 4-5 MeV.

6.2 Final Simulation Results and Comparison with Micromegas Detector Measurements

As described in Section 4.1, the Micromegas module used for this thesis was irradiated with the Am-Be source for three years prior to the measurements taken in this thesis (Vogel et al. 2023). The detector set-up during the irradiation period was set-up as shown in Fig. 6.11, with the Am-Be source placed immediately in front of it. This set-up was changed to measure the current drawn from the detector by placing the neutron source 25 mm away from the detector, for placing different thicknesses of lead. Fig. 6.12 shows a schematic of the same, with 5 lead slabs of 5 mm thickness placed between the source and the detector.

Fig. 6.13 shows the simulation results of the sum number of electrons created in the drift region as well as those reaching the drift region from the other layers. This figure already accounts for the ratio factor R≈450 between the 60 keV photons and the 4.4 MeV gammas. The total number of electrons extracted from the simulation is expected to have a similar trend to the current measured from the detector since it is proportional to the number of electrons produced by the source radiation in the drift region. On multiplying the number of extracted electrons per second by a mean gas gain of $7.5 \cdot 10^3$, we obtain the total charge per second, i.e. the current for different thicknesses of lead.

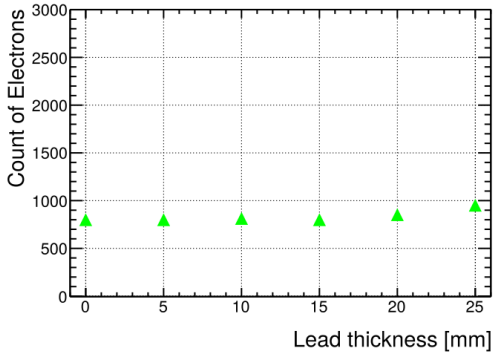

FIGURE 6.9: Geant4 simulation: Number of electrons reaching or created in the drift region from 1-10 MeV neutrons, weighted to the intensity distribution and rounded off to the nearest integer. The number of extracted electrons remains unaffected by the change in lead thickness.

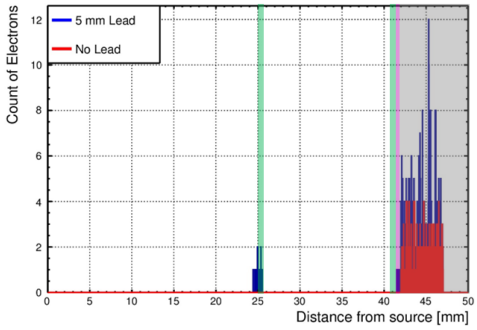

FIGURE 6.10: Geant4 simulation: Position of the electrons created that reach the gas in the no lead and 5 mm lead simulations for 5 MeV neutrons. The grey box indicates the drift region while the magenta and green boxes signify copper and FR4 respectively. Just before the first layer of FR4, a 5 mm lead slab is placed for one of the simulations. Few electrons created in lead from x=24 to x=25 mm manage to reach the drift region.

The measured current drawn from the detector can be seen in Fig. 6.14b. This current can be attributed completely to the irradiated particles from the source. Fig. 6.14a is compared to Fig. 6.14b, which shows the measured current drawn from the detector. In comparison with the experimentally measured current drawn from the detector in Fig. 6.14b, the simulated current in Fig. 6.14a is much lower than the current drawn with the contributions from the 60 keV photons with no lead.

Since the number of 60 keV photons entering the depends on the intensity ratio R of the gammas which was determined with an HPGe detector (see chapter 5.2) and used for the simulation, an in-depth investigation is required to establish the accuracy of the value since a lot of uncertain factors like the efficiency of the HPGe detector, the dimensions of the detector crystal and its geometry, which were all unknown, must be considered. The polynomial fit used for determining the efficiencies must also be tested since the efficiencies of the 4.4 MeV photons were

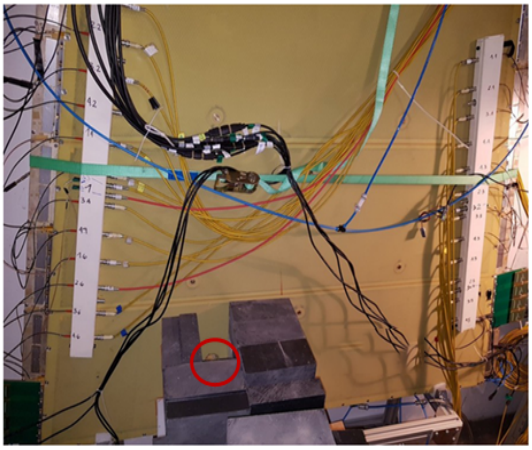

FIGURE 6.11: Micromegas Detector set-up with neutron source placed right in front of it, shielded from all the other sides by lead and borated plastic.

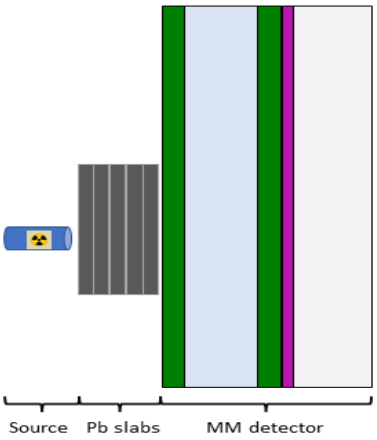

FIGURE 6.12: Schematic of the detector set-up to measure current from the source. 5 lead slabs of 5 mm thickness were placed between the source and the detector.

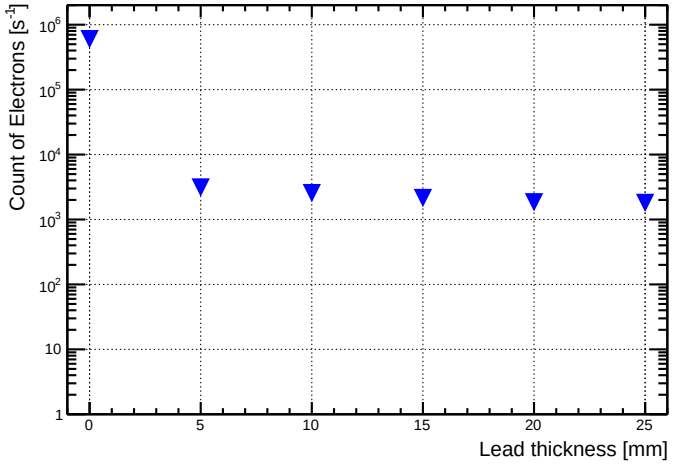

FIGURE 6.13: Total number of electrons extracted from all the radiated particles from the source per second. The ratio factor R determined with the Ge detector for the 60 keV photons to the 4.4 MeV gammas is implemented at 0 mm of lead. After 5 mm of lead, the contribution from the 60 keV photons completely gets attenuated.

extrapolated and any errors in the higher range will have a big influence on the ratio, which directly affects the 60 keV photon contribution.

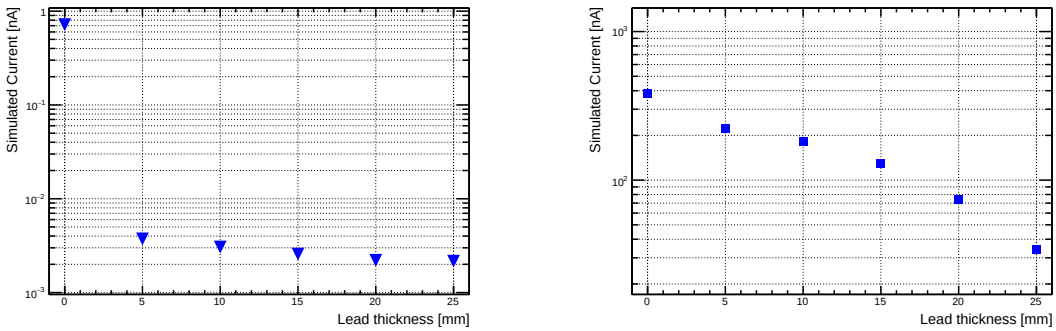

(a) Geant4 simulation: Total contributions from the, 60 keV photons, 4.4 MeV gammas and the 1-10 MeV neutrons radiated from an Am-Be source for different thicknesses of lead.

(b) Measurement: Current is drawn from the Micromegas detector for different thicknesses of Lead. The contribution from the 60 keV photons are implicitly assumed to have completely absorbed on placing 5 mm of lead.

FIGURE 6.14: Fig. 6.14a shows the Geant4 simulation results of the corresponding current to the number of electrons reaching the drift region or created in the region by the 4.4 MeV photons and the 1-10 MeV neutrons over the increasing thickness of Lead. Fig. 6.14b is the measured current from the detector from the neutron source radiation.

After 5 mm of lead, the 60 keV photons and their contributions are completely attenuated. The simulated current is also below the measured current by a factor of 10^4. However, on performing a linear fit on the currents simulated and measured for lead thickness 5 to 15 mm, it is observed that the simulated current has a linear behaviour like we would expect while the measured current does not [Appendix C]. This indicates some underlying mechanism that exists for the 4.4 MeV photons or the MeV neutrons in the lead that the simulation doesn't account for. This can arise with possible material impurities in lead or interactions in materials like the mesh or the graphite material of the anode which aren't considered in the simulation.

In conclusion, the simulation design behaves the way it was expected to in terms of the interactions of the photons and neutrons with the detector layers. The 60 keV photons get completely attenuated after placing 5 mm of lead. The contribution from 4.4 MeV at 5 mm of lead is expected to be higher than at no lead because of the Compton scattered photons having a higher cross section in copper and argon, while the contribution from the neutrons is unaffected by the lead thickness. However, some underlying mechanisms are unaccounted which are beyond the scope of this thesis. This opens up several possibilities to test the Geant4

simulation using other suitable physics lists for particle interactions, especially neutron-matter interaction, which might show higher precision.

Chapter 7

Summary and Outlook

A Micromegas module was irradiated with an Am-Be source emitting neutrons and gammas for a period of three years. In order to test the resilience and performance of the detector after the long-term irradiation, measurements were performed for this detector with gas mixtures Ar:CO_2 in 93:7 vol.% and Ar:CO_2 : iC_4H_{10} in 93:5:2 vol.% for different voltage scans.

In case of potential damage to the anode due to long-term irradiation, the performance of the detector in terms of spatial resolution and tracking efficiency in the irradiated region is expected to deviate from the performance in the non-irradiated region. The track reconstruction method was used to determine the track properties of the detector. This method uses the precision coordinates of the reference layers to determine the expected hit position in the layer under investigation. The difference in the expected cluster position and the measured cluster position is considered the residual of that layer and is fit to a bi-Gaussian fit where the core Gaussian defines the resolution of the inner detector and the tail Gaussian explains the broadening of the tails due to the δ-electron distribution.

For the inner eta layer at amplification voltage 530 V in Ar:CO_2 : iC_4H_{10}, core and the weighted residuals were estimated to be 139 μm and 244 μm respectively. These are satisfactory residuals considering the fact that cosmic muons have an angular spectrum, which influences the reconstructed position of all the layers. Although the influence of the angle of inclination has been corrected for the layer under investigation using the time-corrected charge-weighted position reconstruction method, the position of the clusters in the precision direction is still determined by the centroid method since there is no external track.

A hit is considered efficient if the absolute residuals of the layer being investigated are less than 5 mm. The 2D efficiency is plotted against the precision and non-precision coordinates of the detector in Fig. 4.12, showing no degradation in the performance of the detector in the immediate vicinity of where the source was

placed for the long-term irradiation period. The efficiency is fit to a first-order polynomial and plotted as a function of the voltage scans taken for the two gas mixtures in Fig. 4.14. The analysis shows that the performance of the detector remains unaffected by this long-term irradiation and the efficiency of the detector remains above 90% for high amplification voltages of the two gas mixtures.

To understand the properties of the Am-Be source used for the irradiation period, a characterisation study is performed. The intensity of the gamma spectrum of the 10 GBq Am-Be source was determined using a Germanium (Ge) detector. The energy and efficiency calibration of the Ge detector was performed with sources with known activity and decay schemes. The relative efficiency is then used to determine the ratio between the 60 keV and 4.4 MeV photons. This value is used in a Geant4 simulation to disentangle the contributions from radiated products of the Am-Be source.

A Geant4 simulation is performed with the geometry given in Fig. 6.1 which has 5 mm thick slabs of lead placed in front of the Micromegas detector to attenuate the contribution from the 60 keV photons. The total number of primary and secondary electrons produced in the gas or reaching the drift region are considered to reach the amplification region. In terms of photon and neutron interactions with the detector layers, the simulation design performs as predicted. Once 5mm of lead is added, the 60,keV photons are fully attenuated. Since Compton scattered photons have a bigger cross section in copper and argon, the contribution from 4.4,MeV at 5,mm of lead is projected to be greater than at no lead and afterwards gets attenuated. The contribution from neutrons is unaffected by lead thickness and stays nearly constant.

The total number of extracted electrons can be correlated to the current drawn from the detector when placed in a similar set-up to the simulation. Since the current drawn must be proportional to the total electrons extracted, the current is calculated for a mean gas gain of $7.5 \cdot 10^3$ and compared to the measured current. The calculated current in Fig. 6.14a is substantially smaller than the experimentally observed current obtained from the detector in Fig. 6.14b. This difference can be attributed to the ratio R (see section 5.2.3), which is dependent on several unknown parameters like the thickness of the crystal and the detector geometry.

The simulated current after 5 mm of lead is also 10^4 less than the observed current. A linear fit is performed on the simulated and measured currents for lead thicknesses ranging from 5 to 15 mm. It is discovered that the simulated current behaves linearly as expected, while the measured current does not. This suggests that there is an underlying mechanism for the 4.4,MeV photons or MeV neutrons

in the lead that the simulation does not account for. This can occur due to probable lead impurities or interactions in materials such as the mesh or graphite material of the anode that are not included in the simulation. While this estimation is outside the scope of this thesis, it presents an opportunity to test the Geant4 simulation with other relevant physics lists for particle interactions, particularly neutron-matter interactions, which may provide greater precision.

Appendix A

Properties of the Calibration Sources

The activity of the calibration sources as of February 2023, when the measurements were taken is as follows:

Energy [keV]	Activity [kBq]
59.54 (^{241}Am)	40
121.8 (^{152}Eu)	33.4
661.6 (^{137}Cs)	189
1332 (^{60}Co)	0.06

TABLE A.1: Intensity distribution of the calibration sources used to determine the energy-dependent efficiency of the HPGe detector.[8]

Intensity distribution of the calibration sources used:

These values are then used in eq. 5.7 to obtain the counting efficiency ε.

[9]Data taken from https://www.gammaspectacular.com/blue/gamma_spectra/

Energy [keV]	Intensity
59.54 (^{241}Am)	0.359
121.8 (^{152}Eu)	0.286
244.7 (^{152}Eu)	0.758
344.2 (^{152}Eu)	0.265
411.1 (^{152}Eu)	0.223
443.9 (^{152}Eu)	0.282
661.6 (^{137}Cs)	0.851
778.9 (^{152}Eu)	0.129
964.1 (^{152}Eu)	0.146
1112 (^{152}Eu)	0.136
1173 (^{60}Co)	0.999
1332 (^{60}Co)	0.999
1408 (^{152}Eu)	0.210

TABLE A.2: Intensity distribution of the calibration sources used to determine the energy-dependent efficiency of the HPGe detector.[9]

Appendix B

Attenuation Coefficients

The attenuation coefficients of the two photon energies 60 keV and 4.4 MeV for different interactions in 100 mm of germanium are given in Table.

Energy [keV]	Photoeffect μ/ρ_{ph} [cm^2/g]	Compton effect μ/ρ_{comp} [cm^2/g]	Pair Production μ/ρ_{pair} [cm^2/g]
59.54	1.770	0.125	0.000
4400	$1.000 \cdot 10^{-4}$	0.024	0.008

TABLE B.1: Intensity distribution of the calibration sources used to determine the energy-dependent efficiency of the HPGe detector.[10]

These values are corresponding to cross sections in an equation given by

$$\sigma = \frac{\mu}{\rho} \cdot \rho \tag{B.1}$$

where ρ is the density of the material. For germanium, ρ =5.323 g/cm^3.

Appendix C

Investigation of Simulated and Measured Current

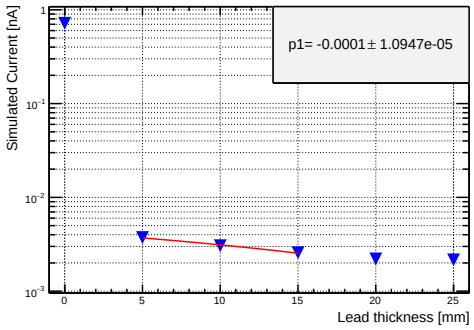

FIGURE C.1: Geant4 simulation: Current simulated for different thicknesses of lead. A first-order polynomial is fit to the current measured at 5, 10 and 15 mm of lead. A good linear fit can be observed, just as expected from the attenuating behaviour of 4.4 MeV gammas.

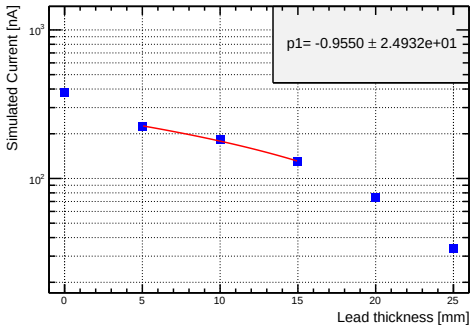

FIGURE C.2: Measurement: Current drawn by the Micromegas detector for different thicknesses of lead. A first-order polynomial is fit to the current measured at 5, 10 and 15 mm of lead. The huge error on the slope determines that the current does not follow a linear curve, indicating some underlying mechanisms the simulation does not factor in.

On comparing the simulated current with the measured current, it is seen that the measured current is higher by a factor of $\approx 10^4$ for the attenuated 60 keV photons. This is investigated by performing a polynomial fit on the current measured from 5 to 15 mm thickness of lead. Since the behaviour of neutrons in increasing lead thickness should remain unchanged, the total electrons reaching the drift region should see an exponential decrease after 5 mm of lead due to attenuation of 4.4 MeV gammas in lead. A first-order polynomial fit is performed here since

the plot is on a logarithmic scale. As expected, the simulated current has a good linear fit but the measured current has a slope error larger than the slope value. This indicates that it is not linear and has some underlying contributions from the neutrons or the 4.4 MeV gammas that is not observed by the simulation.

Acknowledgement

At this point, I would like to thank the people that supported me during the past year:

- I want to thank Prof. Dr. Otmar Biebel for giving me the opportunity to write my master thesis in his group and giving me interesting insights on various topics even beyond physics.
- I would like to thank Dr. Ralf Hertenberger for proofreading my thesis even while at CERN and especially for his unending support and guidance regarding my work.
- I would like to thank my advisor Fabian Vogel for proofreading my thesis, for the incredible support he has provided and for showing me the ropes in a completely new environment.
- I would like to thank the entire team: Christoph Ames, Dr. Valerio D'Amico, Florian Egli, Stefanie Götz, Dr. Christoph Jagfeld, Lars Linden, Dr. Alexander Lory, Katrin Penski, Maximilian Rinnagel, Nick Schneider, Celine Stauch and Dr. Chrysostomos Valderanis for providing a fun and dedicated working environment.
- Last but not least, I would like to thank my family for their constant support even from thousands of kilometers away.

Bibliography

Agostinelli, S. et al. (2003). "Geant4—a simulation toolkit". In: *Nuclear Instruments and Methods in Physics Research Section A: Accelerators, Spectrometers, Detectors and Associated Equipment* 506.3, pp. 250–303. ISSN: 0168-9002. DOI: https://doi.org/10.1016/S0168-9002(03)01368-8. URL: https://www.sciencedirect.com/science/article/pii/S0168900203013688.

Alexopolous, T. et al. (2015). *Stereo Information in Micromegas Detectors*. Tech. rep. Geneva: CERN. URL: https://cds.cern.ch/record/2052206.

BEARDEN, J. A. and A. F. BURR (Jan. 1967). "Reevaluation of X-Ray Atomic Energy Levels". In: *Rev. Mod. Phys.* 39 (1), pp. 125–142. DOI: 10.1103/RevModPhys.39.125. URL: https://link.aps.org/doi/10.1103/RevModPhys.39.125.

Berger M.J., Hubbell J.H. (2010). In: XCOM: Photon Cross Section Database (version 1.5). [Online] Available: http://physics.nist.gov/xcom [2023, June 24].

Bjørnstad, Tor (June 2021). "Modern Industry: Neutron Basic Interactions, Sources and Detectors for Materials Testing and Inspection". In: pp. 372–391. ISBN: 9780124095489. DOI: 10.1016/B978-0-12-819725-7.00087-8.

Blum, Walter, Luigi Rolandi, and Werner Riegler (2008). *Particle detection with drift chambers*. Particle Acceleration and Detection. ISBN: 978-3-540-76683-4, 978-3-540-76684-1. DOI: 10.1007/978-3-540-76684-1.

Bortfeldt, Jonathan (Apr. 2014). "Development of floating strip micromegas detectors".

Cockcroft, John Douglas (1955). "Experimental Nuclear Physics". In: *Nature* 175, pp. 53–54.

Croft, S. (1989). "The use of neutron intensity calibrated 9Be(α, n) sources as 4438 keV gamma-ray reference standards". In: *Nuclear Instruments and Methods in Physics Research Section A: Accelerators, Spectrometers, Detectors and Associated Equipment* 281.1, pp. 103–116. ISSN: 0168-9002. DOI: https://doi.org/10.1016/0168-9002(89)91221-7. URL: https://www.sciencedirect.com/science/article/pii/0168900289912217.

Davisson, C. M. (Jan. 1965). "Interaction of γ-RADIATION with Matter". In: *Alpha-, Beta- and Gamma-ray Spectroscopy*. Ed. by Kai Siegbahn. Vol. 1, p. 37.

Flierl, Bernhard (Apr. 2018). "Particle tracking with micro-pattern gaseous detectors". URL: http://nbn-resolving.de/urn:nbn:de:bvb:19-221980.

Giomataris, Y. et al. (1996). "MICROMEGAS: a high-granularity position-sensitive gaseous detector for high particle-flux environments". In: *Nuclear Instruments and Methods in Physics Research Section A: Accelerators, Spectrometers, Detectors and Associated Equipment* 376.1, pp. 29–35. ISSN: 0168-9002. DOI: https://doi.org/10.1016/0168-9002(96)00175-1. URL: https://www.sciencedirect.com/science/article/pii/0168900296001751.

Gray, P.W. and A. Ahmad (1985). "Linear classes of Ge(Li) detector efficiency functions". In: *Nuclear Instruments and Methods in Physics Research Section A: Accelerators, Spectrometers, Detectors and Associated Equipment* 237.3, pp. 577–589. ISSN: 0168-9002. DOI: https://doi.org/10.1016/0168-9002(85)91069-1. URL: https://www.sciencedirect.com/science/article/pii/0168900285910691.

Herrmann, Maximilian Georg (Oct. 2019). "Series calibration of segmented and multi-layered micromegas modules for ATLAS".

Iodice, M. (Feb. 2015). "Micromegas detectors for the Muon Spectrometer upgrade of the ATLAS experiment". In: *Journal of Instrumentation* 10.02, p. C02026. DOI: 10.1088/1748-0221/10/02/C02026. URL: https://dx.doi.org/10.1088/1748-0221/10/02/C02026.

Jones, L (2001). *APV25-S1: User guide version 2.2*. Chilton: RAL Microelectronics Design Group. URL: http://cds.cern.ch/record/1069892.

Kawamoto, T. et al. (June 2013). "New Small Wheel Technical Design Report". In.

Klein, O. and Y. Nishina (Nov. 1929). "Über die Streuung von Strahlung durch freie Elektronen nach der neuen relativistischen Quantendynamik von Dirac". In: *Zeitschrift für Physik* 52.11, pp. 853–868. ISSN: 0044-3328. DOI: 10.1007/BF01366453. URL: https://doi.org/10.1007/BF01366453.

Kleinknecht, K. (1998). *Detectors for Particle Radiation*. Detectors for Particle Radiation. Cambridge University Press. ISBN: 9780521648547. URL: https://books.google.de/books?id=RI05DW7rtmMC.

Klitzner, Felix (2019). "Development of novel two-dimensional floating strip micromegas detectors with an in-depth insight into the strip signal formation". PhD thesis. Munich U. DOI: 10.5282/edoc.24286.

Knoll, G F (1979). "Radiation detection and measurement". In: URL: https://www.osti.gov/biblio/6642801.

Landau, Lev Davidovich (1944). "On the energy loss of fast particles by ionization". In: *J. Phys.* 8.4, pp. 201–205. URL: https://cds.cern.ch/record/216256.

Leo, William R. (1994). "Passage of Radiation Through Matter". In: *Techniques for Nuclear and Particle Physics Experiments: A How-to Approach*. Berlin, Heidelberg: Springer Berlin Heidelberg, pp. 17–68. ISBN: 978-3-642-57920-2. DOI: 10.1007/978-3-642-57920-2_2. URL: https://doi.org/10.1007/978-3-642-57920-2_2.

Lösel, Philipp (2017). "Precision Calibration of Large Area Micro Pattern Gaseous Detectors". Presented on 2017-07-24. URL: https://cds.cern.ch/record/2640188.

Martoiu, S et al. (Mar. 2013). "Development of the scalable readout system for micro-pattern gas detectors and other applications". In: *Journal of Instrumentation* 8.03, p. C03015. DOI: 10.1088/1748-0221/8/03/C03015. URL: https://dx.doi.org/10.1088/1748-0221/8/03/C03015.

Raether, H. (1964). *ELECTRON AVALANCHES AND BREAKDOWN IN GASES*. URL: https://books.google.de/books?id=gSwnwQEACAAJ.

Ramsauer, Carl (Mar. 2006). "Über den Wirkungsquerschnitt der Gasmoleküle gegenüber langsamen Elektronen". In: *Annalen der Physik* 369, pp. 513–540. DOI: 10.1002/andp.19213690603.

Rossi, Bruno and Kenneth Greisen (Oct. 1941). "Cosmic-Ray Theory". In: *Rev. Mod. Phys.* 13 (4), pp. 240–309. DOI: 10.1103/RevModPhys.13.240. URL: https://link.aps.org/doi/10.1103/RevModPhys.13.240.

Scholer, Patrick (2021). "Tracking Performance of Micromegas chambers for the ATLAS New Small Wheel project". Presented 07 Mar 2022. URL: https://cds.cern.ch/record/2839930.

Stelzer, Bernd (2016). "The New Small Wheel Upgrade Project of the ATLAS Experiment". In: *Nuclear and Particle Physics Proceedings* 273-275. 37th International Conference on High Energy Physics (ICHEP), pp. 1160–1165. ISSN: 2405-6014. DOI: https://doi.org/10.1016/j.nuclphysbps.2015.09.182. URL: https://www.sciencedirect.com/science/article/pii/S2405601415006719.

Tanabashi, M. et al. (Aug. 2018). "Review of Particle Physics". In: *Phys. Rev. D* 98 (3), p. 030001. DOI: 10.1103/PhysRevD.98.030001. URL: https://link.aps.org/doi/10.1103/PhysRevD.98.030001.

Townsend, John Sealy Edward (1910). *The theory of ionization of gases by collision [microform] / by John S. Townsend*. English. Constable London, xi, 88 p. :

Vogel, Fabian (2024). Thesis work in progress.

– (2022). "Test of ATLAS Micromegas detectors with ternary gas mixture at the CERN GIF++ facility". In: *PoS* EPS-HEP2021, p. 757. DOI: 10.22323/1.398.0757.

Vogel, Fabian et al. (2023). "Long term neutron irradiation studies of square meter sized resistive strip micromegas detectors". In: *Nucl. Instrum. Meth. A* 1045, p. 167653. DOI: 10.1016/j.nima.2022.167653.

Declaration of Academic Integrity

I hereby declare that this thesis is my own work, and that I have not used any sources and aids other than those stated in the thesis.

Eshita Kumar

Munich, 19.07.2023